MPHIL

Biological and chemical sensing at terahertz frequencies

Mohamad Hashim, Siti Norbaieah

Award date:
2017

Awarding institution:
University of Bath

BIOLOGICAL AND CHEMICAL SENSING AT TERAHERTZ FREQUENCIES

Siti Norbaieah binti Mohamad Hashim

A thesis submitted for the degree of Master of Philosophy

University of Bath

Department of Physics

April 2017

COPYRIGHT

Signature: 

ABSTRACT

This thesis present the studies of terahertz applications including measuring water content in leaf sample and guided wave components, aimed at the development of next-generation terahertz systems. In chapter 2, a study of the methods for measuring leaf water content using terahertz time domain spectroscopy measure continuously the water content status of the sample. A few different wavelengths of a near infra-red LED as 1450 nm, 875 nm, 1050 nm, and 1200 nm also were used in this experiment to make a comparison of the method that fits best for measuring the water status. In chapter 3, a physical structure of a microstructured capillary as an optical waveguide that guides electromagnetic waves in the optical region as a function of the transport medium is discussed in term of mode profiles and attenuation. In chapter 4, perforated thin nickel films with periodic conical hole arrays were used to study the surface modes and the excitation of spoof surface plasmon polaritons is demonstrated in the terahertz transmission spectra of the periodic sub wavelength hole arrays. Surface modes can be supported by both metallic surfaces with different nonlinear dispersion curves which result in spectral interferences in a near field region when the surface modes couple out of the waveguide into free space. In this thesis; the THz waveguides is used to explore the guiding mechanism of an anti-resonant optical waveguide.

ACKNOWLEDGEMENT

I would like to thank to many people during my work for the MPhil study. It has been a great privilege to spend 3 years and half in the Department of Physics at University of Bath and its member will always remain dear to me.

Special note of appreciation to my supervisor, Steve Andrews for giving me this opportunity to undertake the study and his patience during my research works and thank you to physics department and the staff, Paul Reddish and Wendy Lambson for their support and helpful suggestion.

Special thanks to my husband Mohamad Ikhram bin Ismail, my lovely children Muhammad Izz and Mohamad Nafis. Thank you for being incredibly person who's always around and understanding my struggle in this journey and for my family for their love and encouragement.

And lastly thank you to my friends, Nurhasmiza Sazalli and family for the lovely life experience and incredibly support.

List of Figures:

List of table:

CHAPTER 1

INTRODUCTION TO TERAHERTZ TIME-DOMAIN SPECTROSCOPY (THZ-TDS)

1.1 Terahertz radiation

Terahertz radiation also known as far infrared radiation or T-rays has frequencies between the high-frequency edge of the millimetre wave band, 100 gigahertz (1×10^{11} Hz), and the low frequency edge of the mid-infrared band, 10 THz which corresponds to wavelengths of radiation in the range from 3 mm to 30μm. It falls in between infrared radiation and microwave radiation and shares some properties with each of these for example, travels in a line, non-ionizing, can penetrate a wide variety of non-conducting materials, can pass through clothing, paper, cardboard, wood, masonry, plastic and ceramics, but cannot penetrate liquid water or metal [1]. Historically this frequency region has been explored for over hundred years.

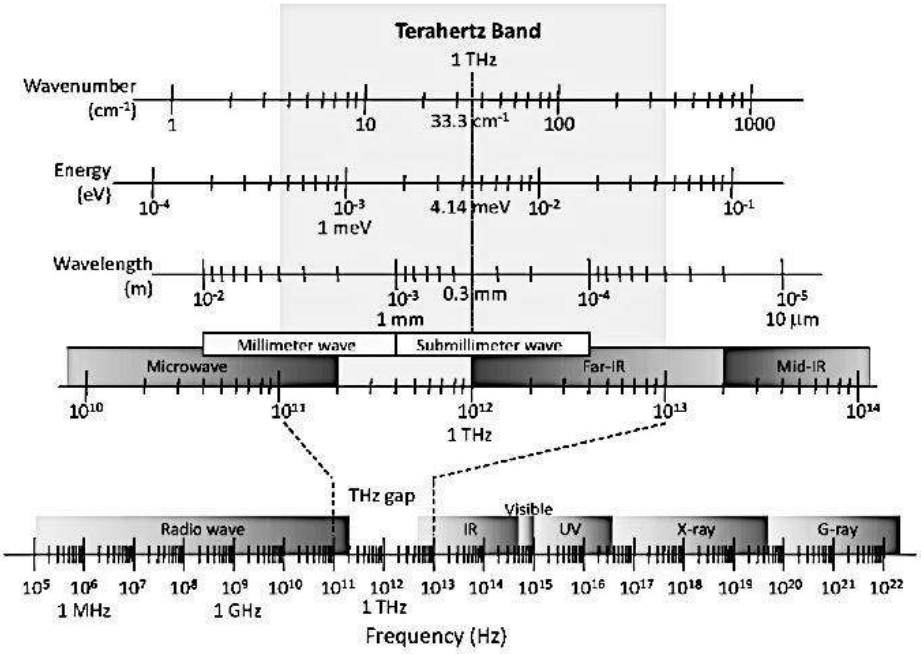

Figure 1- 1: Terahertz band in electromagnetic spectrum [2].

Figure 1-1 illustrates the THz band in the electromagnetic spectrum, where THz band merges into neighbouring spectral bands such as millimetre-wave band, which is the highest radio frequency. These bands are distinguished by their characteristics technologies. Microwave emitters and sensors are solid-state or vacuum tube electronic applications that rely on optical and thermal devices [2]. The so-called "THz-gap" arises from the nature of the sources and detectors used in spectroscopy both at the optical (high frequency) side and electronic (low frequency) side of the gap and it's because of 20-30 years ago, these were few technologies for the generation and detection or manipulation

of radiation in this region One THz corresponds to a photon energy of 4 meV (33.3 cm^{-1}) [3].

Sources of THz are commercially available, for example optically pumped gas lasers and backward wave oscillators, operated in continuous wave mode with up to tens of miliwatt output power [4]. Solid state devices such a s Gunn Diodes with Schottky-diode multiple chains can generate hundreds of GHz [5]. Quantum cascade lasers (QCL) are narrow-band emitters which exploit intersub-band transitions in quantum well structures [6], and since 1980s the developments in ultrafast lasers, broadband, optically excited pulsed source of THz have been started.

1.2 Terahertz time-domain spectroscopy (THz-TDS)

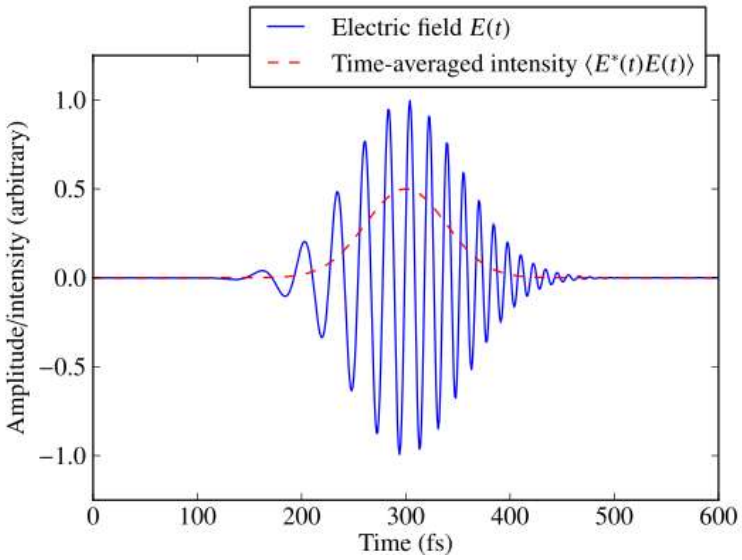

Figure 1- 2: A positively chirped ultrashort pulse of mid-infrared in the time domain [2].

Historically, terahertz spectroscopy has been hindered by the low brightness of incoherent far infrared sources and the poor sensitivity and low speed of bolometric detectors. With the advent of THz-TDS, these difficulties are overcome in a radical way. THz-TDS is a spectroscopic technique that allows the time resolved measurement of light matter interaction with broadband and powerful THz pulses using femtosecond lasers. The THz transients are single-cycle like and typically less than 1 ps in duration. Their spectrum spans the range from below 100 GHz to more than 3 THz. The brightness of the THz transients exceeds that of conventional thermal sources

and the coherent detection is orders of magnitude more sensitive than bolometric detection.

Broadband pulses of THz radiation are coherently generated and detected using ultrafast laser pulses with a time resolution of a few hundred femtoseconds. The generation and detection are sensitive to the sample and effects on both the amplitude and the phase of the THz radiation. This technique can provide more information than Fourier transform spectroscopy that is only sensitive to the amplitude and gives phase information although it is a tricky technique [2]. Fourier transform of the time-domain signal gives both spectral amplitude and phase information which allows probing of the real and imaginary parts of the dielectric function of materials. Extremely high signal-noise ratios of up to 10^6 in electric field make the technique very powerful despite the low source power of typically a few micro watts.The advances in the efficiency of THz transmitter and receivers and improved designs have led to the extension of Terahertz time-domain techniques to real-time imaging. Optically gated detection allows direct measurements of the THz electric field with a time resolution of a fraction of a picosecond. From this measurement both the real and imaginary part of the dielectric function of a medium may be extracted [7].

THz-TDS is also known as a technique of combination setup of broadband generation and detection. This combined set up measures the change in both amplitude and phase of THz pulses induced by a sample, which

provides enough information to simultaneously determine the absorption and dispersion of the sample by analysing the Fourier transforms of the waveforms. In THz-TDS, THz pulses are measured both with and without a sample. The basic experimental scheme used for generation and detection of THz pulses using a femtosecond laser is similar to the pump-probe technique. The optical beam is split into two parts, pump and probe arm, one of which is a retro reflector on a motorised translational stage to provide a relative time delay. The optical pump pulse illuminates the emitter and generates the THz pulses, which travel through a distance in free space before being focused on the detector. The detection of THz pulse is achieved in a photoconductive antenna by accelerating free carriers induced by the probe pulse with the THz field. THz pulses can generated in THz-TDS by either transients currents in a photoconductive antenna or by difference frequency generation in a nonlinear crystal [2].

1.3 Photoconductive (PC) antenna generation

This photoconductive antenna (PC) is the key component in the most of THz-TDS [8]. It exploits the increase in electrical conductivity of semiconductors when they are exposed to light. THz radiation can be generated from a biased PC antenna exited by femtosecond laser pulses. In general; a PC transmitter consists of two metal electrodes deposited on a semiconductor substrate and does not incorporate a resonant antenna. Photo carriers generated

in the gap are accelerated by an applied static bias field. A standard material for PC antenna is low-temperature grown GaAs (LTG GaAs) which has a band gap of 1.43 eV [9]. In the emitter, photo carrier are excited between two metal strip electrodes that a coated on a GaAs substrate [10]. The photocarriers will be accelerated by an applied static bias field and produce a transient photocurrent. The current density is described as

$$J(t) = N(t).e.V(t) \tag{1.1}$$

where N, is the density of photocarriers, e is the elementary charge and V is the electron velocity. The photocarriers density N is a function of time, is determined by the laser pulse shape and the carrier lifetime, where the time dependence of the carrier density $N(t)$ is given by,

$$\frac{dN}{dt} = G(t) - \frac{N(t)}{\tau_c} \tag{1.1}$$

where $G(t)$ is the carrier generation rate of the laser pulse and τ_c is the carrier trapping time (~100 ps for semi-insulating Gallium Arsenide (SI-GaAs) and ~1 ps for LT-GaAs). Since the photocurrent varies in time, it generates an electromagnetic pulse, whose electric field is given in the far field by

$$E_{THz} \propto \frac{\partial J(t)}{\partial t} \tag{1.2}$$

The THz electric field can be written as

$$E_{THz}(t) \propto \frac{\partial N(t)}{\partial t} V(t) + N(t) \frac{\partial V(t)}{\partial t} \tag{1.3}$$

where, factors contributing to the performance of PC antenna are the substrate material, bias field, geometry of the active area and antenna and excitation laser pulse [10]. Commonly, non-resonant antennas are used but the spectral intensity can be modified using resonant antennas such as dipoles.

1.4 Photoconductive (PC) antenna detection

The electric field of a THz pulse is measured in a detector that is simultaneously illuminated with THz area gated by an ultra-short laser pulse as shown in Figure 1-3. Two common detection schemes are used in THz-TDS systems are photoconductive (PC) sampling and electro-optical-sampling. The PC detection system is similar to the mechanism for generation of THz. It is based on a micron-scale antenna with a very short carrier lifetime (sub-ps) and high resistance semiconductor in a gap between the antenna arms. THz pulses are focused on the antenna and generate a bias electric field. A photocurrent is induced when the photo conducting gap is simultaneously illuminated by an

optical gating pulse that increase the conductivity. The short carrier lifetime is to keep the coverage resistance of the photoconductive gap by remaining carriers. This is essential to keep the noise low because the noise current is proportional to $1/\sqrt{R}$. This photocurrent created by the THz electric field is amplified using a low-bandwidth current to voltage converter that produce a voltage roughly proportional to the THz electric field [11]. The detector will produce a different electrical signal depending on whether the detection pulse arrives when the electric field of the THz pulse is low or high. An optical delay line is used to vary the timing of the detection pulse. In order to enhance the signal-noise-ratio, the signal is processed by a lock-in amplifier synchronized with an optical intensity modulator in the pump beam at 2.5 kHz such as an optical chopper.

The photocurrent induced by the THz field $t(\omega)$ can be expressed by the relation below:

$$\bar{J}(\omega) = N(\omega).\mu(\omega).t(\omega).H(\omega).E(\omega) \tag{1.5}$$

where 1& is the density of photo generated carriers created by the probe beam. This depends on the probe beam pulse width and the carrier lifetime in the photoconductive material. μ( ) is the frequency dependent mobility of photogenerated electrons. W& is the complex amplitude transmission coefficient for the GaAs-air interface. & is the ratio of the terahertz electric

field at the receiver to the terahertz electric field at the transmitter and depends on the THz optical system.

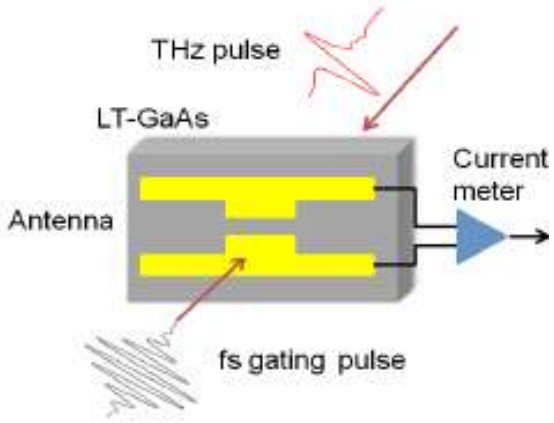

Figure 1- 3: Schematic representation of THz pulse detection with a PC receiver. The laser pulse excites free carrier in the photoconducting gap and the incident THz electric field generates a net current [12].

Figure 1-4 shows the photolithographic process used to manufacture the photoconductive terahertz devices. The photoconductive transmitters and receivers were made using standard photolithography techniques. A chip is first spin-coated with resist and then soft baked to harden the resist and improve adhesion. The chip is exposed to ultraviolet light under a contact mask and the photoresist is developed followed by removing of oxide layers from the sample surface to improve the metal contacts and adhesive. Metallisation is performed using a thermal evaporator followed by lift-off. In this project, Ti/Au (15/150 nm)

metallisation was used. To ensure easy metal lift-off in the final step, the sample was inserted in chlorobenzene prior to developing.

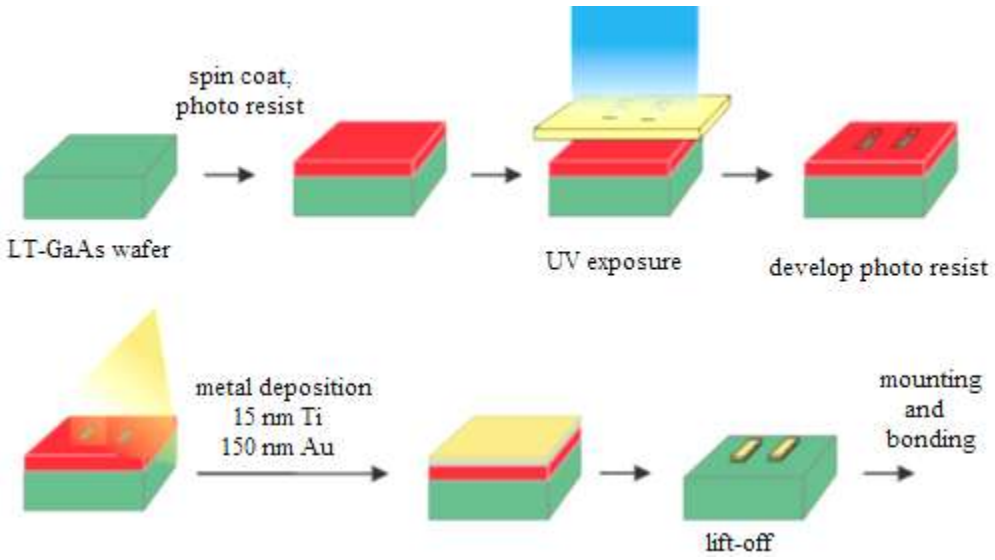

Figure 1- 4: Photolithographic process used to manufacture the PC THz devices.

1.5 Performances of Photoconductive (PC) Detector

THz detectors for time-domain systems were intensively studied in the 1990s, and now GaAs grown at low temperature is the most common material used as a photoconductive antenna [12, 13]. The important properties are mobility and carrier lifetime. Long carrier lifetimes will permit the reception of large amounts of noise and short carrier lifetimes will reduce the mobility and signal level.

Table 1- 1: Properties of photoconductive receivers. The measurements are based on averages on several devices.

Material	Carrier lifetime (ps)	THz mobility ($cm^2V^{-1}S^{-1}$)	Resistivity
LT-GaAs	0.5	~3000	50 kΩcm

From the table 1-1 above, it shows that Low-temperature grown GaAs (LTG-GaAs) is a semiconductor material with high carrier mobility and a fast carrier capture time. The THz mobility is around 3000 and impedance minimum for gated device resistance average is 1μΩ. This makes LT-GaAs materials attractive for applications such as ultrafast switches and THz antennas, application for which it is desirable to have the highest possible mobility [14]. Since the hole mobility in LT-GaAs is one order of magnitude lower than the electron mobility, carrier transport in the THz frequency range is dominated by electrons.

1.6 Substrates Lenses: Collimating Lens and Hyper-Hemispherical Lens

A refractive index-matched high-resistivity hyper-hemispherical silicon lens was positioned on the back of receiver substrate with a thin interceding layer of paraffin oil as shown in Figure 1.5 below. The total internal reflection in this substrate prevents most of radiations from escaping into free space. This is solved by the substrate lens because most radiation can exit close to normal

incidence at lens surface. Therefore, a substrate lens, attached to the backside of a PC emitter to collimate the THz radiation, is a critical component for an efficient THz emitter. The substrate lens is made of high resistivity silicon because the refractive index matches well with GaAs substrate materials, the linear absorption is very low at the THz frequencies, dispersion over the whole THz spectrum is almost negligible and the fabrication of high-quality components is reasonably simple [2].

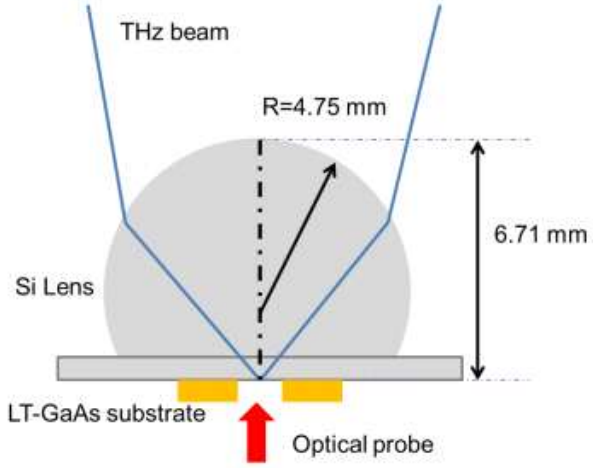

Figure 1- 5: A hyper-hemispherical lens attached to the receiver substrate for focusing THz radiation [16].

1.7 Hollow-core fibre coupled Terahertz time-domain spectroscopy (THz-TDS)

A fibre couple THz-TDS system as shown in Figure 1-6 was used to study the propagation of THz electromagnetic radiation in microstructured capillary waveguides and for measuring and monitoring leaf water content. In this system, the laser pulses are delivered to photoconductive devices via hollow-air-core photonic crystal fibres (HC-PCF). A mode-locked Ti: Sapphire laser was optically pumped by a continuous-wave (cw) argon-ion laser with 8W average output power. The output power ~ 1W and the wavelength were chosen to be 779 nm so that the negative dispersion of the fibre compensates the positive dispersion. The laser beam passes through an optical isolator to prevent feedback to the laser. Then, the laser beam is divided by a beam splitter into two parts of the pump (generation) and probe (detection) and passes through a beam expander and ×20 objectives lens in each beam path. Half-wave plates are used to minimize the effect of the unintentional birefringence of the fibre arising from artefacts fabrication the coupling efficiency from the free space to the fibre output can reach 60%.

An optical chopper is used to modulate the pump beam at 2.5 kHz for lock-in detection. A real time THz signal is acquired using fast scanning retro-reflector and displayed on an oscilloscope. The average power used for THz generation is 80 mW. The output from the fibre is collimated and then focused onto the photoconductive transmitter. The probe laser pulse can be used to gate

either a conventional receiver or a near-field probe. The optical gating powers are for the 20 mW for the far field receiver and 8 mW for the near field probe. The transmitter is a conventional co-planar waveguide design with 50 µm PC gaps and the receiver is a 10µm dipole antenna. Both devices are made using LT GaAs as the PC material.

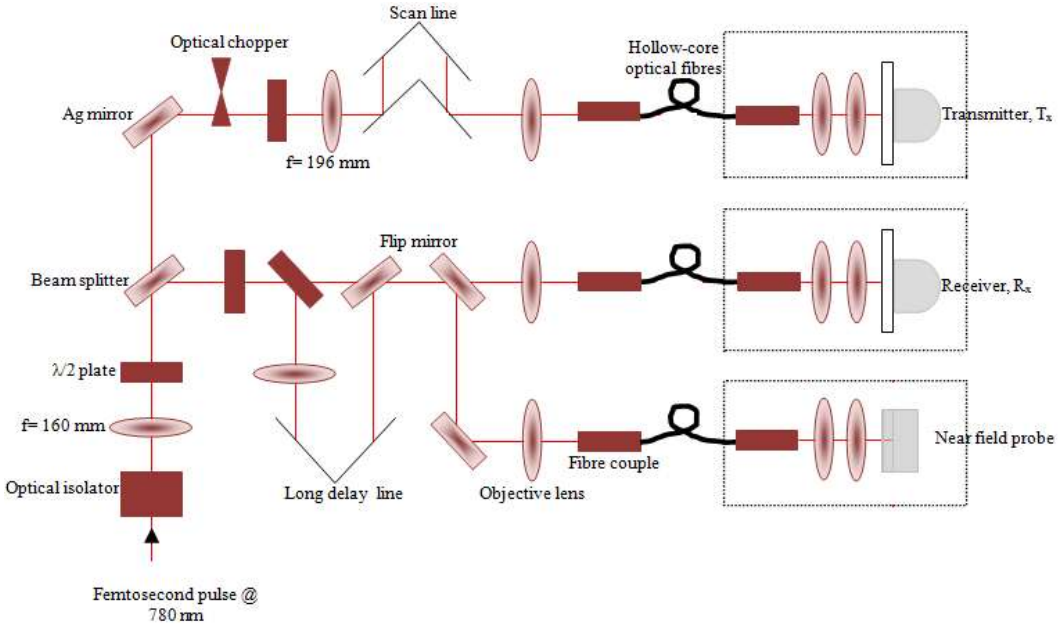

Figure 1- 6: Schematic of fibre-coupled THz-TDS setup.

1.8 Near-field probe

Near field probe as shown in Figure 1-7 is used in order to improve the image resolution by letting the THz beam passing through an aperture with a size similar to the incident wavelength. The aperture was made from a 50 µm thick brass sheet and placed ~2 cm in front of conventional receiver's silicon

lens. A high resistivity silicon wafer with 600 μm thickness was inserted between the Si lens and the receiver to improve the beam collection efficiency. Nevertheless, the disadvantage is the limitations of the propagating of the pulse through the small aperture and the strong attenuation with amplitude $\propto d^3$ and for the sub wavelength aperture, the high cut off frequency is $\upsilon_c \propto d^{-1}$. This limitation can be overcome by measuring the electric fields just behind the aperture in the very near-field region less than *d* away from the aperture.

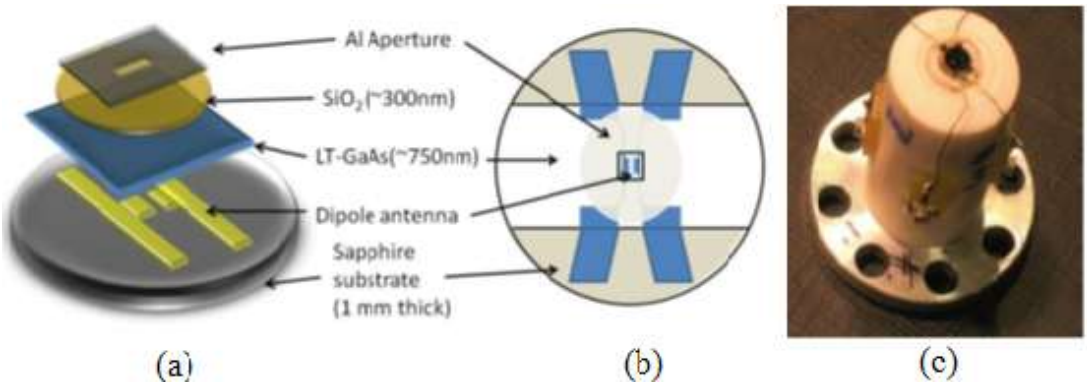

Figure 1- 7: (a) Three-dimensional view of the near field probe structure used in this experiment. (b) Schematic diagram of a top view of the terahertz near field probe. Blue areas indicate the metal and grey shows polished facets of sapphire (c) Picture of near field probe mounted on a ceramic holder with integrated focusing lens [15].

1.9 Imaging with THz pulses

Pulsed THz imaging is accomplished by raster-scanning of a target at the focal plane of a THz-TDS system as shown in Figure 1-8. Changes in the amplitude $A(x, y)$ and the phase $\emptyset(x, y)$of the THz pulses map out the spatial inhomogeneity of the target, characterized by material properties such as refractive index $n(x, y)$, absorption coefficient $\alpha(x, y)$ and thickness $d(x, y)$. Figure 1-9 shows, each pixel of a THz-TDS image contains a whole waveform in the time domain. In the time domain, the maximum amplitude $A_a(x, y)$ or the arrival time $t_a(x, y)$of the waveform is typically used to form a 2D image. If the target material has a complicated dispersion relation, a wavelet analysis can reveal important properties of the sample. Frequency domain imaging is also possible with the spectrum of the waveform obtained by the Fourier transform [2].

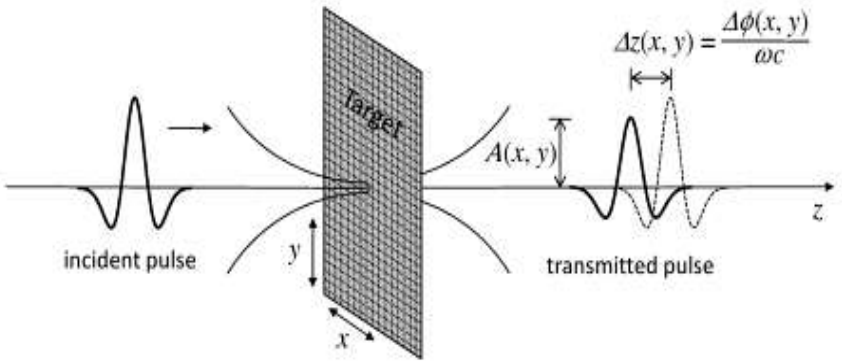

Figure 1- 8: Raster scan imaging with THz pulses in transmission geometry [2].

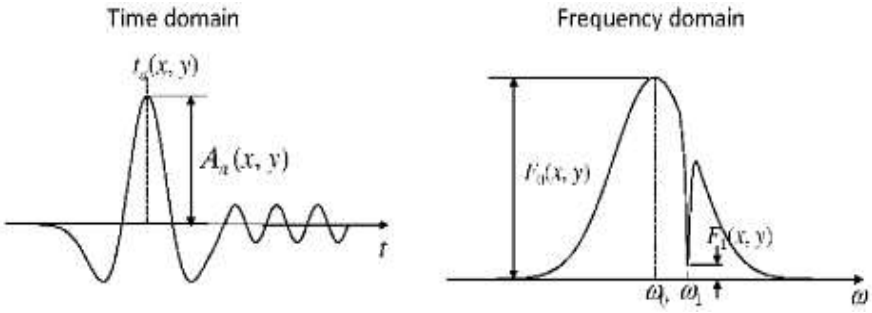

Figure 1- 9: Display options for THz-TDS imaging: maximum amplitude A_a (x, y) and arrival time ta (x, y) in the time domain, maximum amplitude F_0 (x, y) and amplitude at resonance F_1 (x, y) in the frequency domain, and total energy $I(x,y) = \int |A(x,y,t)|^2 dt$ [2].

1.10 Application of THz and Terahertz Time Domain Spectroscopy (THz-TDS)

THz-TDS system is a spectroscopic system for characterisation of materials such as semiconductor, superconductor and dielectrics. A recent promising application is in food sciences field where is the detection of protein content is reviewed for application in food safety, medicine and health [16]. In quality control, for non-contact and non-destructive inspections, near field imaging and THz microscopy offer a better spatial resolution determined by the aperture size and does not suffer from a waveguide cut-off [17] for example THz non-destructive evaluation (THz-NDE)[18], homeland security[18], quality control of food and agricultural product[18], global environmental monitoring and ultrafast computing [18].

References

1. Sokolnikov, A.U., *Introduction,* in *THz Identification for Defense and Security Purposes: Identifying Materials, Substances, and Items*. 2013, World Scientific. p. 1.

2. Lee, Y.-S., *Principles of Terahertz Science and Technology*. 2009, Springer: Oregon, USA. p. 1-9.

3. Dexheimer, S.L., *Terahertz Spectroscopy: Principles and Applications*, in *Terahertz Spectral Region*. 2008, CRC Press Taylor and Francis Group: New York. p. 1.

4. Dobroui, A., C. Otani, and K.Kawase, *Terahertz-waves sources imaging applications.* Measurement Science & Technology, 2006. **17**: p. R161-R171.

5. Saeedkia, D. and S. Safavi-Naeini, *Terahertz Photonics: Optoelctronic Techniques for Generation and Detection of Terahertz Waves.* Journal of Lightwave Technology 2008. **26**: p. 2409-2423.

6. Williams, B.S., *Terahertz quantum-cascade lasers.* Nature Photonics, 2007. **1**: p. 517-525.

7. Martin C. Nuss, J.O., *Milimeter and Submilimeter Wave Spectroscopy of Solids.* 1998.

8. Grischkowsky, M.V.E.a.D.R., *Characterization of an optoelectronic terahertz beam system.* IEEE Transactions on Microwave Theory and Techniques, 1990. **38**: p. 1684-1691.

9. Jan-Martin Ramer, F.O., Georg von Freymann and Rene Beigang *Generation and detection of terahertz radiation up to 4.5 THz by low-temperature grown GaAs photoconductive antennas excited at 1560 nm.* Applied Physics Letters, 2013. **103**(021119): p. 1-4.

10. Xi-Cheng Zhang , J.X., *Generation and Detection of THz Waves*, in *Introduction to THz Wave Photonics*. 2009, Springer US. p. 27-31.

11. Cheville, R.A., *Terahertz Time-Domain Spectroscopy with Photoconductive Antennas* in *Terahertz Spectroscopy: Principles and Applications*, S.L. Dexheimer, Editor. 2008, CRC Press. p. 1-15.

12. Tonouchi, M., *Cutting-Edge Terahertz Technoloy*. Nature Photonics, 2007. **1**: p. 97-105.

13. R. Yano, H.G., Y. Hirayama, S. Miyashita, Y. Kadoya et al., *Terahertz wave detection performance of photoconductive antennas: Role of*

antenna structure and gate pulse intensity. Journal of Applied Physics, 2005. **97**(103103): p. 1-6.

14. Matthew C. Beard, G.M.T., and Charles A. Schmuttenmaera, *Subpicosecond carrier dynamics in low-temperature grown GaAs as measured by time-resolved terahertz spectroscopy.* Journal of Applied Physics, 2001. **90**(5915): p. 1-10.

15. Yi.Pan, *Terahertz time-domain spectroscopy and near-field imaging of microstructured waveguides*, in *Physics*. 2013, Univeristy of Bath: University of Bath. p. 108.

16. Lijuan Xie, Y.Y., Yibin Ying, *The Application of Terahertz Spectroscopy to Protein Detection: A Review.* Applied Spectroscopy Reviews, 2014. **49**(6): p. 448-461.

17. *Terahertz*, in *Encyclopedia of Nanotechnology*, B. Bhushan, Editor. 2012, Springer Netherlands. p. 2653.

18. Tonouchi, M., *Sate-of-the-Art of Terahertz Science and Technology*. 2014, Springer. p. 153-166.

LIST OF FIGURES:

CHAPTER 2

2.1 Introduction to use of Terahertz radiation in water detection.

One special characteristic of the terahertz (THz) frequency range (300 GHz to 3 THz; 100 μm to 1 mm) (i.e., picosecond timescale), is the strong attenuation of terahertz (THz) radiation by water which makes it very sensitive to hydration and to the state of tissue that exhibiting an absorption peaks [1]. Recently research revealed that the Terahertz technology can provide a new alternative form of non-invasive tool or an excellent non-contact probe for measuring and monitoring the water content of leaves and plants [2] because of water is strongly absorbed in the terahertz band while the dehydrated biological tissue is partially transparent. Linear transform [3] and effective medium theory [4] may be used for measuring three different categories either wet, dry or very dry for a leaf. Although useful and informative, most of the methods normally used to measure water content in plant tissues imply damage or separation of the organs of interest from the plant and resulting unachievable real-time changes of water content measurement. In THz region, the strong attenuation by the water of the samples makes these samples completely opaque and its turns out to be very convenient method to measure the water content of a thin sample such as a plant leaf. The transmission signal from a dry leaf has an influence so the attenuation of the signal so can be used directly for a qualitative observation of the leaf's water content. Water is highly absorptive in the THz range, while most materials which absorb moisture are either very transparent or reasonably transparent to THz. Consequently the

high contrast between dry biomass and liquid water resulting a high absorption coefficient in the THz frequency range [2].

The number of NIR or MIR applications is continuously increasing especially to predict qualitative and quantitative of agricultural product as substitute of conventional destructive method. The NIR spectra quality is impacted by various factors such as physical state of the sample. In a previous study, the detection of plant water stress using near infra-red (NIR, 0.7 – 1.3 μm) and middle infra-red (MIR, 1.3-2.5μm) by remote sensing has been proposed to test the ability of the leaf water content to determine leaf relative water content (RWC) of different species with natural variation in RWC from water stress is only about 20% [5]. Kristen-Vizi et al. showed a good correlation was found in between red reflectance and leaf water potential as well as green reflectance and leaf water potential but this methodology is suitable for estimating coarsely in a large area and expensive for daily usage [6]. Gillon et al., works on the relationship between the water content of leaves and their spectral properties using NIR (400- 2500 nm) [7].

2.2 Why monitoring drought stress

Water stress has major implications for global supply chains, especially within the major growth economies. This damage causes losses in the agricultural production. The purpose of measuring of leaf water content is very significance for all aspect of plant science as well as research in plant biology. Specific tool for non-invasive measuring and monitoring of drought stress resistant plant is available as a commercial product. Technically, to monitor drought stress, it can be categorized as either destructive or non-destructive method. Based on

absorption and reflection of electromagnetic radiation but there has a significant drawback for example, in the microwave range, the result is strongly influenced by the inorganic salt content in the leaves, and the resolution of the image is limited due to large wavelength. The most reliable methods used for non-destructive quantification of the leaf water content are based on spectroscopy between 0.75 µm and 100µm corresponding to frequencies between 400 THz and 3THz and infrared spectroscopy of between 1- 2 µm [8].

Leaf discoloration shows nutrient deficiencies, for example over fertilization, lack of water and disease. If the plants don't get enough with ample water, they will have a sign of drought stress like brown and shrivelled leaves. For example, a raspberry plant need one to two inches of water per week during season and 4 inches during the harvest period and quantifying drought stress normally means low 20 % water reduction from turgid state [9].

2.3 Measuring THz transmission

In this study, the setup measurement was discussed in chapter 1. Briefly, the electromagnetic radiation was emitted from a small gap in a transmitter antenna. By using the lenses, the diverging radiation was bundled into a beam and focused on a small spot. The rays emanate from the sample received by a receiver of the same type. The resulting THz radiation generates an electric current that depends on both amplitude and the phase of the incident THz waves. The current detected at the receiver antenna was in the range of nanoAmpere (nA). The low power of THz ensures that the leaves could be

measured over a long time period without getting any damages such as burning.

2.4 Material and methods

2.4.1 Thermogravimetric measurement

Thermogravimetric method is a very useful and important method which provides information about physical and chemical phenomena of an organic sample by measure changes in the weight loss (mass) of sample. Analysis of the thermal activity which causes changes in physical and chemical properties of a material are measured as a function of time to be used to characterize the sample [10].

2.4.2 Plant material

There are three types of leaves were used in this experiment which are raspberry, tomato, and beech. The leaf sample was a straight cutting from the plant and promptly wrapped in moist paper to avoid stress. The sample was conserved in the cool box and then, weighed immediately to get the fresh saturated leaf weight where the sample is at full hydration level. For the actual dry weight of the sample, after detaching, the sample was weighted using a balance. After the experiment was done, the sample was put in the lab oven for 36 hours at 110 ºC and was weighed again for the determination of the dry weight and the water content was calculated. The sample weight was measured via thermogravimetric measurement and in the experiment, the leaf mass was continuously monitored using a load cell.

Leaf thickness plays an important role in leaf or plant. These characteristics determine the amount of light absorbed by a leaf and the diffusion pathway of CO_2 through its tissue. On the other hand, it also can be used as a tool to screen species cultivars for productivity. Techniques of leaf thickness estimation are used because of the difficulty to measure it accurately and the time consuming. The variation of leaf thickness between leaves or plant is one of factors affecting the ability to obtain percentage of water spectroscopically. In near-IR spectroscopy, we try to overcome the problem of variation in thickness by rationing different wavelength of NIR source. Thickness and errors can be minimized by averaging a number of readings of the leaf exposed by the beam and by calibrating the THz transmission to water content.

RWC in leaf tissue is commonly used to assess the water status of plants. RWC estimates in leaves from full rehydrated were slightly below 100%, measuring the water content based on fresh and dry mass. The measurement are referred to [11];

$$\text{RWC}\ (\%) = \left(Fresh\ weight - Dry\ weight \Big/ Dry\ weight \right) * 100$$

Leaf area is one of the important variables for most ecophysiological studied concerning light interception, evapotranspiration, and irrigation response. In order to get an estimation of leaf area a nondestructive method using a graph paper was introduce by using an equation [12];

$$Leaf\ area\ (cm^2) = \frac{weight\ of\ the\ leaf\ outlined\ on\ milimetre\ graph\ paper, x}{weight\ of\ the\ one\ cm^2\ of\ the\ graph\ paper, y}$$

In this experiment, the average weight of fresh raspberry leaf used in this experiment is 0.200 ± 0.001 g and average dry leaf weight is 0.040 ± 0.001 g, for tomato leaf and beech leaf is 0.550 ± 0.001 g and 0.350 ± 0.001g for fresh leaf and 0.070 ± 0.001 g and 0.090 ± 0.001 g for dry leaf correspondingly. The average of the leaf area used in this experiment is 790 mm^2 with 80% of relative water content.

2.5 Measuring relative leaf water content with Terahertz

Plants which are not saturated with enough with water and lead to water stress condition. The investigation of water status for different leaves is so beneficial for the irrigation and the distribution of water in plant leaves. Normally the method for determining the leaf water content can be dividing into two types; a destructive and non-destructive. The thermogravimetric is a destructive method. The measurement is done by evaluated the weight differences of the fresh and fully dried weight.

Others method that have been applied for the measurement of leaf water content in the lab, for example Nuclear Magnetic Resonance (NMR) have the disadvantage that electromagnetics and high currents are need to be used and it is far away impossible to design and develop the portable measuring system which can be used on field. Others option left are microwave and infrared spectroscopy. The disadvantage of using the microwave spectroscopy is because of the permittivity value is so depends on of the salinity of the water in the leaf. Infrared spectroscopy gives a promising method for measuring water content in a leaf. The THz frequency region which is 0.1-10 THz has giving an

interesting result of research activity in the field of physics, chemistry, and biomolecules. It is between the mm waves for infrared bands.

The special characteristics of this region can be used to identify an unknown biological and chemical substances and it is a non-contact probe which is a non-destructive technique approach. Because THz radiation is sensitive to water, where the electromagnetic radiation is strongly absorbed by water molecules. The transmission of THz through the leaves depends on total absorption which is depends on optical path length of water. So, as the leaf is stress, the amount of water in a leaf is reduced so do the optical length of water.

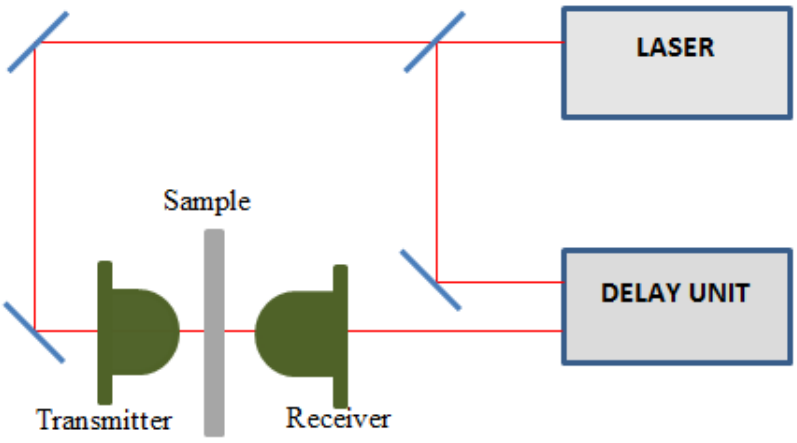

Figure 2- 1: Experiment set up of measuring raspberry leaf water content with THz radiation. A laser emits short pulses of light, which are used for generation and detection of THz.

Figure 2-1 above shows a general scheme of an experiment set up of electromagnetic THz radiation of transmitter and varies of electric current based on the intensity of the THz radiation measured by the receiver. From this data, the THz transmission of raspberry leaf sample is calculated and any phase

shifting of the THz transmission can be determined. Water is strongly absorbed terahertz radiation, while non-polar organic material does not. Therefore a transmission measurement is a very effective way for the quantification of the water present in leaves. The samples were placed in a dry air experiment (< 5% of relative humidity).

In this experiment, the leaf was put on the flat surface in a special holder so the measurement is contact-free which helps to keep a leaf in defined position and to keep the mechanical stress on the sample at a minimum. For each measurement with a sample, a reference measurement is performed without a sample to record the characteristic of measurement set up as shown in figure 2-2 (a). The properties of the sample can be calculated by comparing the result of the sample measurement to a reference measurement. The result in the figure shows that the THz pulse is attenuated and retarded by the sample. Frequency dependent data evaluation is performing in figure 2-2 (b) by applying a Fourier Transform to the time domain data.

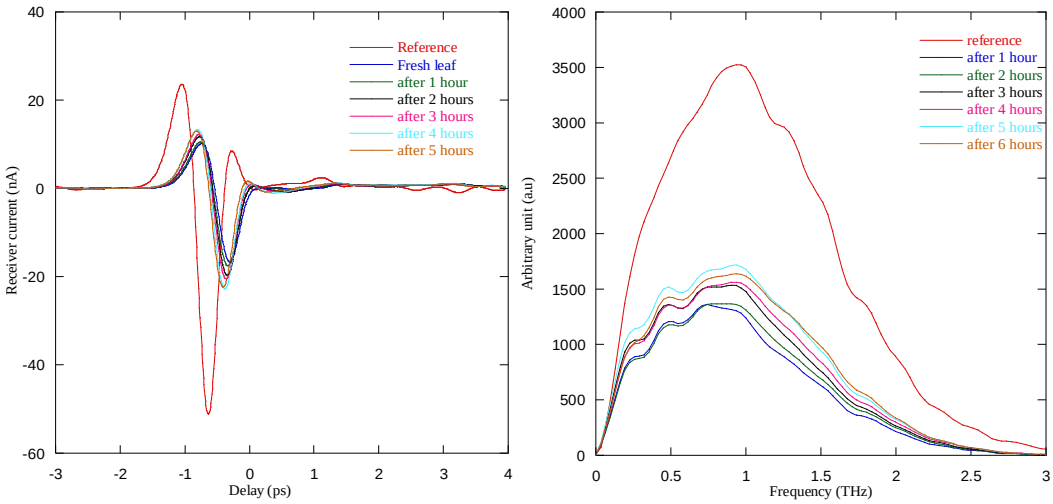

(a) (b)

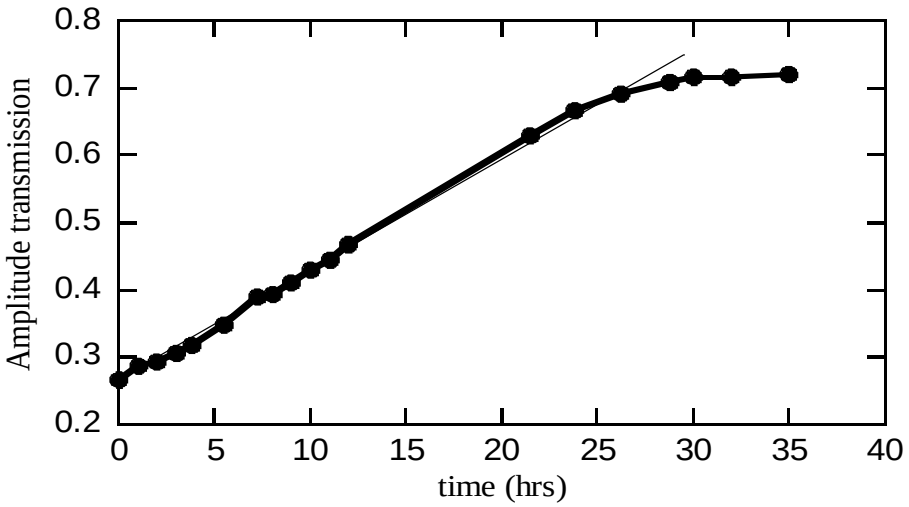

(c)

Figure 2- 2:(a) THz time-domain of THz transmission comparison through raspberry sample for 5 hours between reference and sample measurement shows that the signal is attenuated and delayed by the sample and (b) Corresponding of transmission as function of frequency and (c)Terahertz transmission through leaf sample which is sandwiched between 50mm HDPE for 35 hours.

THz transmission data set was taken over a five hour period from the leaf sample of raspberry as shown in figure 2-2 (a) and the transmission delayed as the leaf was getting dryer. Each line represented the measurement of THz transmission of each hour. It means that the signal is less attenuated and delayed by the leaf sample as the leaf getting dries. After five hours without watering the signal attenuated by the sample is increasing as showed in the graph and its means the water content leaf in that sample is decreasing. Calculated transmission as a function of a frequency determined by the reference pulse the pulses measured every each hour showing that transmittance was low at the earlier time and increased over the time as showed in Figure 2-2 (c).

A single transmission of terahertz radiation through a detached leaf sample where is placed in between 50 mm HDPE was observed for 35 hours in a dry air environment. The result in figure 2-2 (c) showed the THz transmission is increased as much as 33 % of the signal for every 5 hours without watering. There is no more change in transmission after 30 hours without watering, indicating that the leaf is by then in its dry state condition.

2.6 Measuring changes in leaf water content by transmission FTIR spectroscopy.

For the fresh leaf condition, strong absorption of light is dominated by photosynthetic pigments at visible spectrum 400 nm to 700 nm. At 700 nm – 1100 nm, strong absorption of biochemical typically found in dry leaves for example, cellulose, lignin and carbohydrate. At this range, the absorption is also influenced by the multiple scattering, internal structures and air-water interfaces. Middle infrared range or short infrared range, 1100 nm-2500 nm, strong absorption is dominant by water in green leaves, which the primary and secondary absorption peak of water at 1450 nm, 1940 nm, 2500 nm, 980 nm and 1240 nm. These optical properties may be used to measure the freshness of some vegetables. The preliminary results of the study showed that the freshness and dry state of the sample using 1450 nm light sources giving a significant result.

The FTIR machine was set up to cover the range of 1200 nm to 2500 nm with a scan speed of 0.5 cm/s to measure the transmission of three different leaves which is raspberry, tomato, and beech. The purpose of this experiment is to identify the absorption peak of water in different leaf sample at the fresh and dry conditions. From the figure 2-3 above, it shows the absorption peak for fresh and dry state condition was at 1450 nm and 1900 nm. A few of wavelength was chosen for a single measurement which is 875 nm, 1050 nm, 1200 nm, 1450nm, and 1550 nm to measure a water loss in the leaf sample at individual wavelength for almost 24 hours from fresh stage to dry stage of the leaf sample.

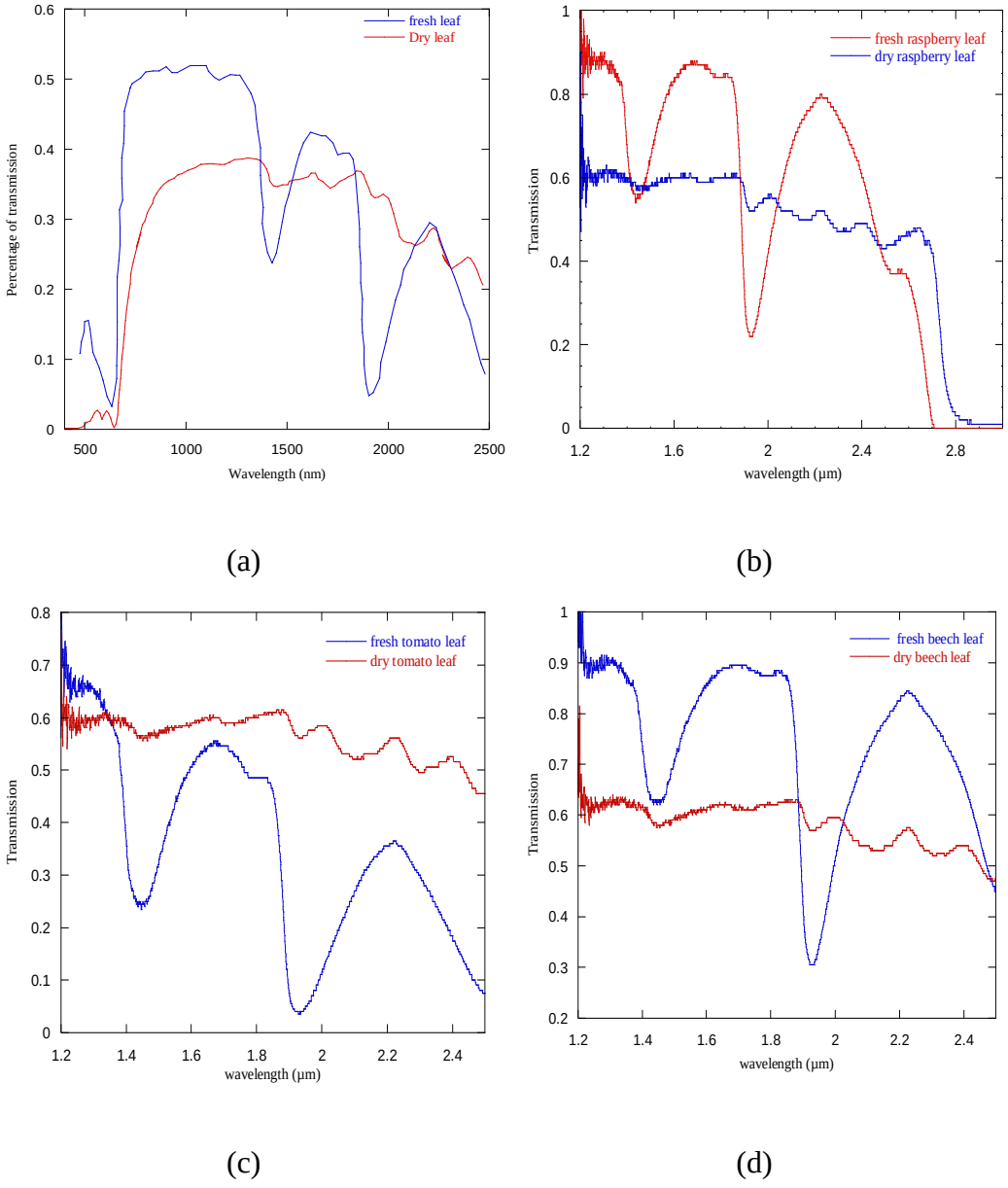

Figure 2- 3: FTIR transmission of different wavelength to different type of leaf (a) Carolina poplar, (b) Raspberry, (c) Tomato, and (d) Beech for a fresh and dry condition.

The relative water content (RWC) was obtained from measuring the dry and fresh weight of the leaf which is for raspberry is 79.30%, 82.03 % for tomato, and 63.02% for beech. The entire graph showed a very clear change of shape between a fresh and a dry state of leaf both at 1450 nm and 1950 nm wavelength, especially for tomato leaf sample. The transmission from a fresh leaf can be differentiated very well regarding the species but for dry leaf, the transmission for the leaf sample is almost the same. A value of relative water content (RWC) of tomato, 82.03% is higher comparing with other samples. It's agreed as shown in figure 2-3 (c) above, the tomato leaf has a very low transmission at 1450 nm which is determined the water absorption peak. A beech leaf sample has the lowest value of RWC, 63.02% and highest transmission percentage 65 % for a fresh condition at the same wavelength. In this experiment, from the figure, the higher value of RWC in the sample, resulting low transmission at 1450 nm water peak absorption and vice versa. The 1450 nm was chosen as a region of interest for water peak absorption based on the water peak absorption result from FTIR.

The thickness of the sample is very crucial because in this experiment tomato leaf has a thicker leaf following by the raspberry and beech. The higher the value of RWC, we can consider the leaf sample is thicker considering the size of the leaf area is almost the same.

2.7 Single Measurement of Leaf Sample

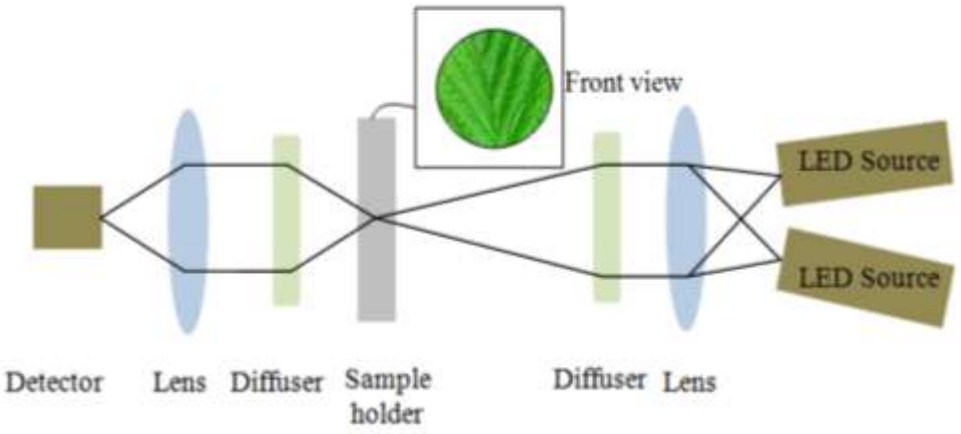

Figure 2- 4: Experimental set up for measuring raspberry leaf water content with LED source with FTIR correspondingly.

Figure 2-4 above shows a general scheme of an experiment set up with a selected LED source with a few of different type of wavelength. The LEDs were modulated at different frequencies and the two lock-in amplifiers were used to detect two different signals. The LED sources used in this experiment are 1450 nm, 1200 nm, 875 nm, and 1050 nm. The source as a transmitter is measured by the detector. From this result, the transmission of a raspberry leaf sample is obtained. Water strongly absorbed at 1450 nm and the other source is more sensitive to another factor like discoloration of the leaf sample as the leaf dehydrated and changed colour. Therefore a transmission of 1450 nm LED source can be used to measure the relative water content but not the absolute value of the water present in leaves.

The raspberry leaf had been subjected to drought stress were monitored periodically as shown in figure 2-5 below determining measuring of

transmission of a few different source type which is THz ~ figure 2-5 (b),1450 nm ~ figure 2-5 (c), 1200 nm ~ figure 2-5 (d), 875 nm ~ figure 2-5 (e), and 1050 nm~ figure 2-5 (f), . The weight of the leaf measured periodically via time is showed in figure 2-5 (a). From the graph, it shown that drought stress related changes in the water content were induced by suspending the watering. The same leaf sample was measured for every hour by analysing the transmission result of the intercalary (middle) leaf area. As expected, the water loss rate is higher during water deprivation in leaves.

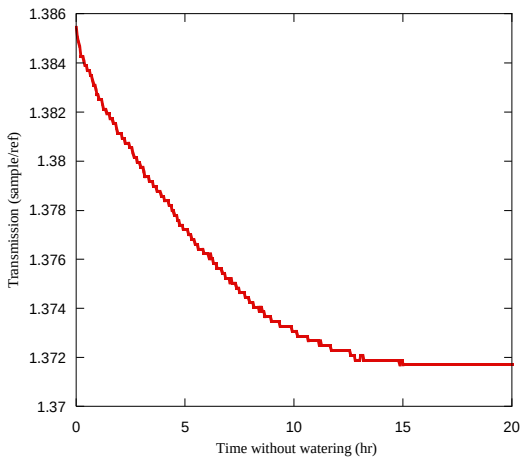
Transmission (sample/ref)
Time without watering (hr)

(a)

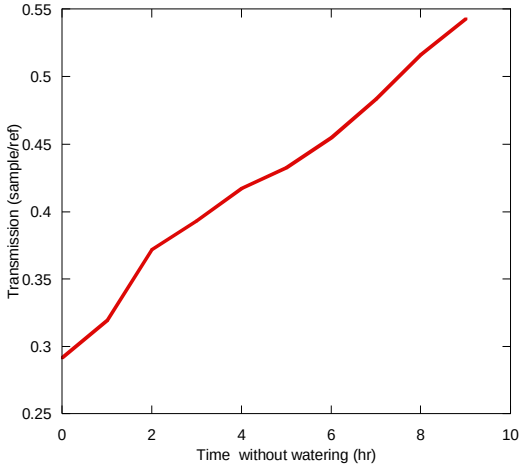
Transmission (sample/ref)
Time without watering (hr)

(b)

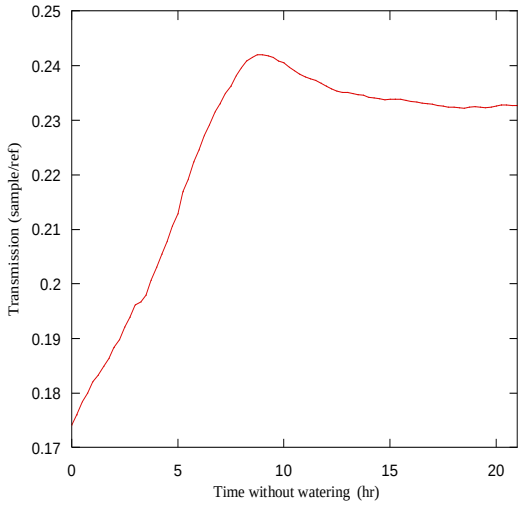
Transmission (sample/ref)
Time without watering (hr)

(c)

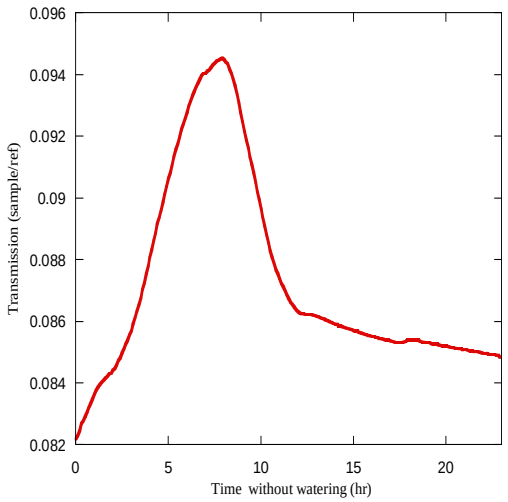
Transmission (sample/ref)
Time without watering (hr)

(d)

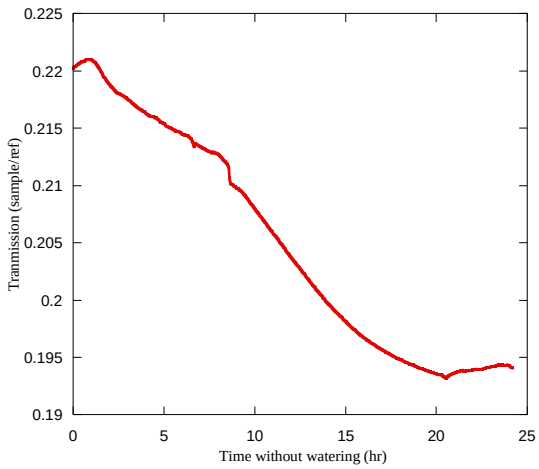
Tranmission (sample/ref)
Time without watering (hr)

(e)

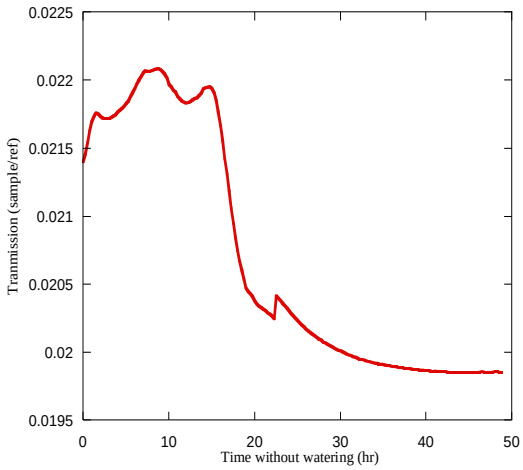
Tranmission (sample/ref)
Time without watering (hr)

(f)

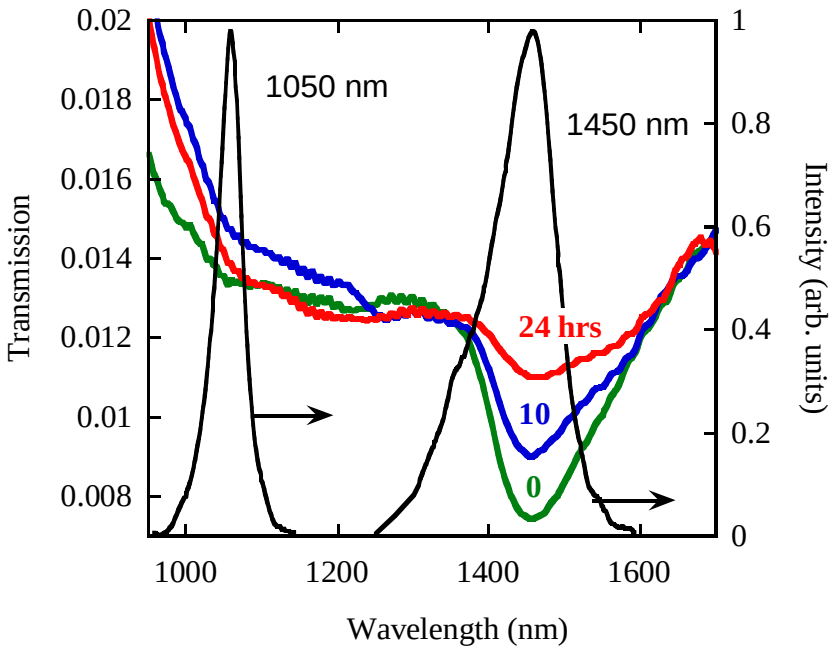

(g)

Figure 2- 5: For this experiment, three leaves were used for each measurement. Leaves were detached from a raspberry plant and their water content was measured repeatedly. Detaching the leaves was necessary for the gravimetric measurements, which were performed for comparison as shows in (a). (b) The gravimetric measurement gives an average value of weight for the whole leaf and other wavelength measurements (c) 1450 nm, (d) 1200 nm, (e) 875 nm and (f) 1050 nm are performed on a small spot at the middle area of the leave. (g) A leaf sample being measured in 3 different conditions which are a fresh state (0 hours), after 10 hours and after 24hours without watering between near infrared range 1000 nm -1800 nm.

The average relative water content for the raspberry sample is around 79.00 % and terahertz transmission frequency range between 0.1 - 3.0 THz with a peak at 0.96 THz. From the result it shows that THz is sensitive in measuring water content in leaf compared to another wavelength. FTIR spectrums showed the water peak absorption at 1450 nm and agreed with the experimental result of raspberry leaf transmission using a 1450 nm LED as shown in Figure 2-8 (c), (g) whereas the transmission signal is good and increase significantly within 20 hours' time observation but then it's losing a weight through time regarding to the water losses in a leaf.

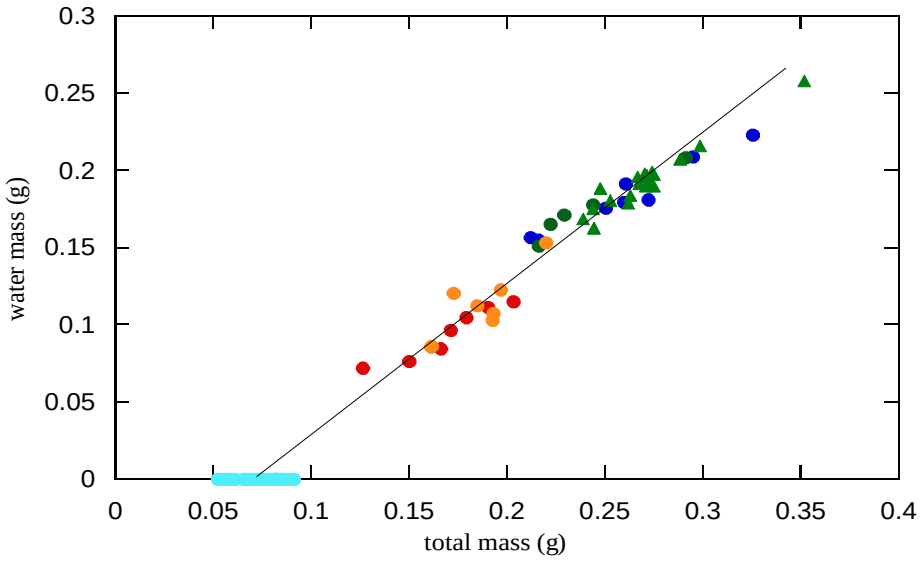

Figure 2- 6: A relation of water mass in gram with total mass in gram for a leaf sample area 875 mm^2 with average dry mass 0.075±0.001 g for four different leaves at varying age.

In this experiment, a raspberry leaf sample was used to study a relation of a total water mass with total mass of the leaf sample. From the graph 2.6 above, it showed that water mass in leaf sample with leaf area size of 875 mm^2 is proportional with the mass of the leaf sample as the leaf dries.

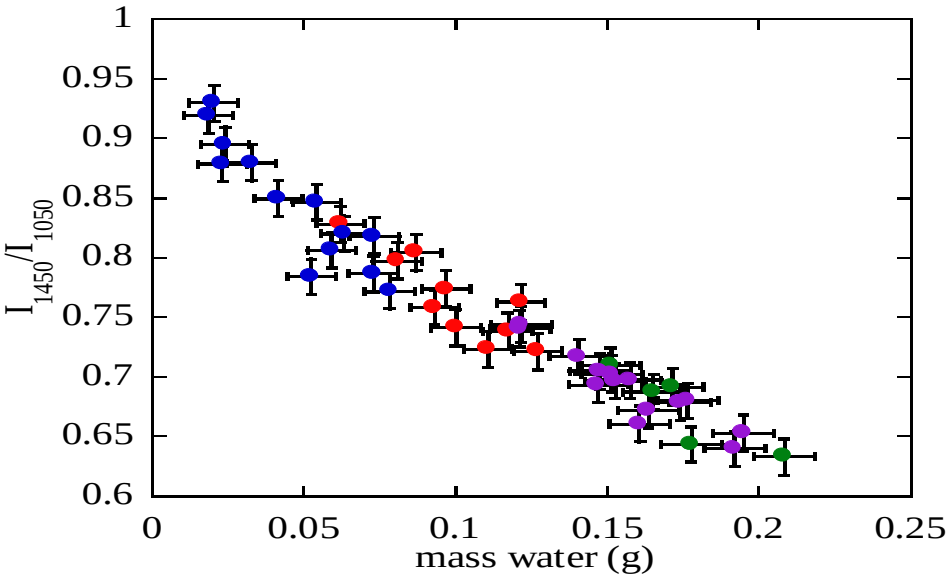

Figure 2- 7: Single measurements near infra-red of different leaf with varying age.

Figure 2-7 shows a single measurement of 1450 nm infrared to a different leaf with relative of water content of 4% at different age. The signal transmission was ratio with 1050 nm infrared to correct a change in leaf thickness and transmission with time/sample. As the signal decreased, the mass water increased, it means that the leaf sample become thinner because of water loss and more signal was transmit through the sample as the sample matured. 1450 near infra- red source is a one of the wavelength which give a significant characteristic of water absorption in a sample.

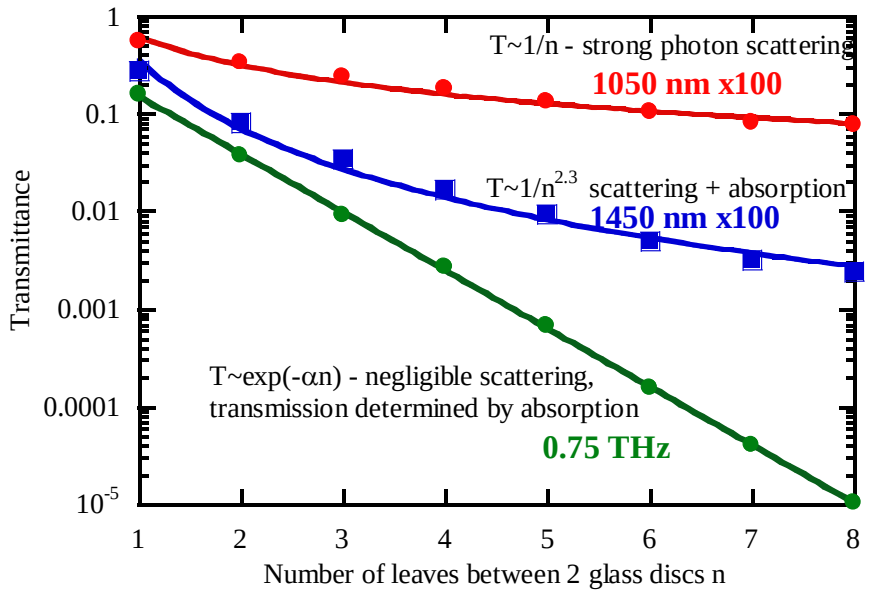

(a)

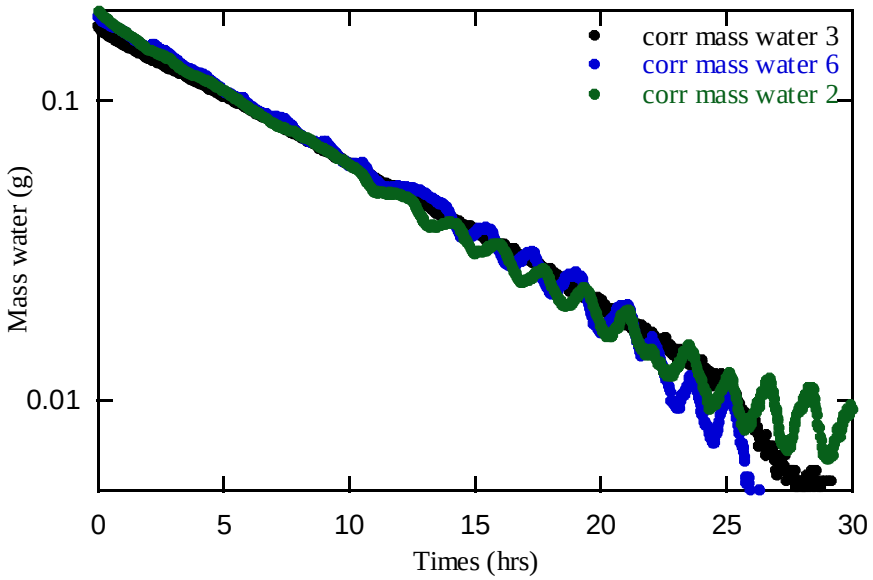

(b)

Figure 2- 8: Transmission of THz, 1450 nm, and 1050 nm LED source through n number of leaves stacking together by being pressed between glass (for infrared) or polyethylene discs (for THz). (b) Correlation of mass water content of time for three different leaf samples in 30 hours of observation without watering.

Near infra-red transmission showed photon diffusion is very important in order to determine water content in leaf sample because at this range of wavelengths light has its maximum depth penetration in tissue. Within this range, photon scattering is dominant in light tissue interaction leads; the propagating light becomes diffused rapidly. From figure 2-8 (a) above, it showed strong photon scattering of 1050 nm transmission and photon scattering plus absorption for 1450 nm LED. The transmission varies with a number of leaves in a stack and varies more slowly in the infrared with thickness than at THz. In THz transmission, the scattering is negligible and the transmission is determined by absorption. The ratio of 1450 nm over 1050 nm near infrared gives reasonable correlation with water mass per unit area when many different leaves with varying water content as showed in figure 2-8 (a). A single frequency for small band of frequencies does not allow for corrections of affect such as variation in leaf thickness from leaf to leaf and from a plant to plant.

2.8 Conclusion

The strong attenuation of terahertz radiation by water makes radiation in this spectral band a highly sensitive non-contact probe of hydration in plants as well as other materials and dielectric materials as a dehydrated biological tissue is mostly transparent in this spectral region allowing measurements of water content of leaves from THz and LED transmission. THz spectroscopy is non-destructive, does not require contact with the sample allows continuous monitoring of leaf water content that could be affected by in vivo water uptake

per water loss processes, therefore giving the unprecedented capability to follow the plant water dynamics same with infra-red transmission.

From the result, it's clearly shown that THz and near infra-red gave a good varies thickness transmission from the single measurement leaf sample in water absorption. The measurement of THz has advantage only if a way of correcting for variation in thickness between leaves can be found that one of the objective of simultaneously measuring THz and IR transmission. Its possibly with a reference of IR wavelength can be found that allows correction. Near infra-red source especially with 1450 nm wavelength as mentioned in previous research is widely used in measuring the water content because of the sensitivity to water content change in a sample but in single leaf measurement, the scattering is weak compares to photon absorption. However, near infra-red with 1450 nm gives an advantage in a correlation of transmission with water content compare to THz transmission. Near infra-red with 875 nm more likely used to measure the pigment and discoloration of the sample and any other biochemical compounds in the leaf sample to measure the deficiencies of the nutrient as the leaf get dries.

Currently, THz-TDS is still a relatively expensive technology but in future, this method can be developed in compact scale, mobile and more cost-effective experimental setups will enable them to be used in a search for selection markers in crop drought improvement programs.

2.9References

1. *Terahertz*, in *Encyclopedia of Nanotechnology*, B. Bhushan, Editor. 2012, Springer Netherlands. p. 2653.

2. Gente, R., and Martin Koch, *Monitoring leaf water content with THz and sub-THz wave.* Plant methods, 2015. **11**(1): p. 1.

3. Hadjiloucas, S., Lucas S. Karatzas, and John W. Bowen, *Measurements of leaf water content using terahertz radiation.* IEEE Transactions on Microwave Theory and Techniques, 1999. **47**(2): p. 142-149.

4. Jordens, C.S., M. Breitenstein, B. Selmar, D. Koch, M., *Evaluation of leaf water status by means of permittivity at terahertz frequencies.* J Biol Phys, 2009. **35**(3): p. 255-264.

5. Hunt, E.R.R., Barrett N, *Detection of changes in leaf water content using near-and middle-infrared reflectances.* Remote sensing of environment, 1989. **30**(1): p. 43-54.

6. Zhang, Q., Q. Li, and G. Zhang, *Rapid determination of leaf water content using VIS/NIR spectroscopy analysis with wavelength selection.* Journal of Spectroscopy, 2012. **27**(2): p. 93-105.

7. Gillon, D., et al., *Estimation of foliage moisture content using near infrared reflectance spectroscopy.* Agricultural and Forest Meteorology, 2004. **124**(1): p. 51-62.

8. Björn Breitenstein, M.S., Mohammad Khaled Shakfa, Thomas Kinder,Thomas Müller-Wirts, Martin Koch, Dirk Selmar, *Introducing terahertz technology into plant biology: A novel method to monitor changes in leaf water status.* Journal of Applied Botany and Food Quality, 2011. **84**(2011): p. 158-161.

9. Strik, B.C., *Growing Raspberries in Your Home Garden*. March 2008, Oregon State University.

10. Januar Parlaungan Siregar, M.S.S., Mohd. Zaki Ab. Rahman and Khairul Zaman Hj. Mohd. Dahlan, *Thermogravimetric Analysis (TGA) and Differential Scanning Calometric (DSC) Analysis of Pineapple Leaf Fibre (PALF) Reinforced High Impact Polystyrene (HIPS) Composites* Pertanika J. Sci. & Technol. , 2011. **19**(1): p. 161-170.

11. Yamasaki, S. and L.R. Dillenburg, *Measurements of leaf relative water content in Araucaria angustifolia.* Revista Brasilleira de fisiologia vegetal, 1999. **11**(2): p. 69-75.

12. Pandey, S.K., & Singh, H., *A simple, cost-effective method for leaf area estimation.* Journal of Botany, 2011. **2011**.

LIST OF FIGURES:

CHAPTER 3

DIELECTRIC THIN-WALL TERAHERTZ WAVEGUIDES

3.1 Introduction

Chemical and biochemical sensing are one of the interesting and promising applications of THz spectroscopy. The interaction between samples and THz radiation may increase using waveguides if the material used is limited. Chemists may use the strong line absorption signatures to differentiate and recognize the sample [1]. The concept of a waveguide is to deliver electromagnetic energy over a long distance taking into account the transmission loss and low dispersion in time-domain measurements. The material absorption of the hollow core guides is low because the power is concentrated in the air core which is transparent to terahertz radiation. Dielectric tube guides are fundamentally multimode and leakage loss increases strongly with mode order. The modes in dielectric hollow core waveguides are described as TE, TM or hybrid.

High index dielectric structures have been demonstrated in plastic ribbon [2] showing that total internal reflection in a dielectric provides another route to guiding THz radiation. However, almost all dielectric material exhibit high material absorption (> 10 dB/m) except for high resistivity single crystal silicon. Hollow core waveguide have been demonstrated with plastic photonic

crystal fibre [3] and capillary [4] with of losses tens dB/m showing that to reduce material absorption, THz waves can be guided in air. The dielectric material should be a low loss material and the thickness has to be accurately designed for optimal transmission at desired frequencies to increase the dispersion of the propagating field.

In this chapter, the study is focused on a dielectric material, microstructured cylindrical silica capillaries with subwavelength thick walls, characterized by waveguide transmission and loss. The microstructuring using stack and draw can easily achieve very thin guide walls. Using the antiresonant optical reflection waveguide (ARROW) principle, hollow core microstructured capillary waveguide structures can be used as guidance for THz radiation with low loss and broadband transmission. The efficiency of waveguides is determined more by the geometry than the material although the material choice does affect the loss and dispersion, as the overlap of the propagating core mode with the guide material is small [4]. This study is more focused on the variable diameter of core dimension in the cylindrically symmetric case. However, the diameter and wall thickness are not easily varied independently for systematic studies. The core-mode and cladding mode are studied in time and frequency domain. The application of waveguides is to transport electromagnetic waves from one point to another [5].

The microstructured waveguides consist of a thick silica capillary outer jacket providing strength of the waveguide for protection from normal handling damage, containing smaller capillaries surrounded the core within an outer jacket known as cladding without a central supporting capillary. This

mechanism only supports leaky modes which is the energy losing gradually to the surrounding cladding and referred as ARROW. This waveguides is useful because it have a low attenuation when the core diameter is larger compared with the wavelength and the wall thickness is small. Another important characteristic of ARROW waveguides is that it is possible to engineer very low field overlap with the dielectric. In this study, silica waveguides allows the transport of high power radiation and guiding at wavelengths where dielectric absorption is significant [6] .

Factors which need to be taken into consideration when choosing the design of THz waveguides are the operating frequency band, the transmission loss, dispersion, physical size flexibility and power handling. In any waveguide design, there is a trade-off between spatial confinement, bandwidth, and attenuation and group velocity dispersion [7] . Waveguides are dispersive due to their geometry and material properties. The group velocity dispersion, D, is defined as

$$D = \frac{\partial}{\partial v}\left(\frac{1}{v_g}\right) \tag{3.3}$$

$$D = -\frac{c}{2\pi\lambda^2}\frac{\partial^2\beta}{\partial\omega^2} \tag{3.4}$$

where, λ is the vacuum wavelength and $v_g = \frac{\partial\omega}{\partial\beta}$ and β is the propagation constant at frequency ω;

$$\beta_{nm} = \frac{2\pi}{\lambda}\left[1 - \frac{1}{2}\left(\frac{u_{nm\lambda}}{\pi d}\right)^2\right] \tag{3.5}$$

$$D = -\frac{c}{2\pi\lambda^2}\frac{\partial^2\beta}{\partial\omega^2} \tag{3.6}$$

At microwave frequencies, metal waveguide exhibits low loss because metals approximate perfect conductors whilst at optical frequencies metals are very lossy but there are many low loss dielectrics materials. At terahertz frequencies, both metals and dielectrics exhibit significant loss in general so that using waveguide concepts in the microwave or optical bands at terahertz frequencies requires careful, application specific design [8].

3.2 Anti-Resonant Reflection Optical Waveguide (ARROW)

Like a Fabry-Perot resonator, which is a pair of partially reflective parallel plates with the reflective surfaces facing each other, the reflected beams from the front and back air-dielectric interfaces interfere. The phase difference between the two beam is given by [9];

$$\delta = \frac{4\pi t}{\lambda}\left({n_f}^2 - {n_0}^2 cos^2\theta\right)^{1/2} - \pi \tag{3.7}$$

where n_f is the refractive index of the dielectric and n_0 is the refractive index of the surrounding medium, θ is the incident angle relative to the film surface. For a small angle θ < 30^o, there is a π phase shift arising from reflections for both TM and TE waves. For destructive interference such as low transmission of waveguide, the phase difference must equal to an odd multiple ofπ, so that,

$$m\pi = \frac{2\pi t}{\lambda}\left(n_f{}^2 - n_0{}^2 cos^2\theta\right)^{1/2}, \text{ where, } m = 1, 2, 3, \quad (3.8)$$

The frequency resonance of the high loss band can be described as,with *t* is the thickness of the silica cladding wall;

$$f_m = \frac{mc}{2t\sqrt{n_f{}^2 - n_0{}^2}} \quad (3.9)$$

where, $m = 1,2,3,\ldots,$, n_f is the refractive index of silica, and n_0 is the refractive index of the air [10]. The bandwidth of the transmission windows is given by,

$$\Delta f = f_m - f_{m-1} = \frac{c}{2t\sqrt{n_f{}^2 - n_0{}^2}} \quad (3.10)$$

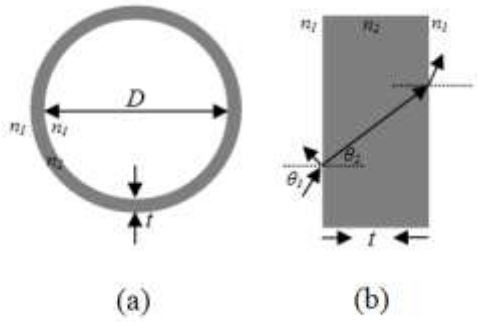

Figure 3- 1: (a) Transverse cross section of a capillary tube waveguide where n1 is air and n2 is a silica. (b) The cladding can be viewed as a Fabry-Perot etalon [10].

The guiding mechanism in this type of leaky guide but is known as anti-resonant reflection optica

3.3 Microstructured capillary tube waveguide

In this study, hollow core microstructured filters are explored for THz wave guiding. These offer flexible control over the guided mode characteristics of loss and dispersion [11].

Silica (SiO_2) is a poor material at terahertz frequencies but the loss in guided wave hollow core fibres is dominated by leakage rather than material absorption. The well-established fabrication techniques for fused silica enable the production of a variety of thin-walled microstructured fibres with engineered properties using the stack and draw techniques [12]. Thin walls are easily obtained, thus shifting resonant to higher frequency whilst easy handling is achieved by suspending the thin walled guiding structure in a thick cladding jacket. At terahertz frequencies, where most dielectric are lossy, hollow cores are preferred because of a large fraction of the power can be confined in the core.

In order to achieve a large bandwidth, high index thin walls are preferable. In this study, THz wave guiding in hollow-core silica microstructured fiber of the type known as antiresonant reflection fibre (ARF) over a frequency range of ~ 1.5 THz. Guidance is achieved by destructive interference of waves reflected from the concentric interfaces surrounding the core. The radiation in the core is inhibited from coupling to the cladding because of a low density of photonic states in the cladding and mismatch of the spatial frequency [11].

Propagation in microstructured capillary tube in which the core is surrounded by one or more concentric rings of tubes within an outer jacket only supports leaky modes which gradually lose energy to the surrounding cladding and radiation and is commonly referred to as anti-resonant reflecting optical wave guiding (ARROW). Although leaky and particularly susceptible to bending loss, hollow core ARROW guides are useful because they can have moderately low attenuation when the core diameter is large compared with the wavelength and the wall thickness is small.

In this work, three samples (A, B, C) of a microstructured capillary waveguide with sub wavelength thick walls were used to study characterization of terahertz propagation. The sample parameter shown in Table 3.1.

Table 3- 1: Parameters of the three microstructured capillary waveguide studi experimentally.

	Length (cm)(±0.01)	Inner diameter (µm)(±0.01)	Outer Diameter (µm)(±0.01)
Sample A	20.7	2110	4970
Sample B	14.9	3078	5400
Sample C	13.6	2056	4300

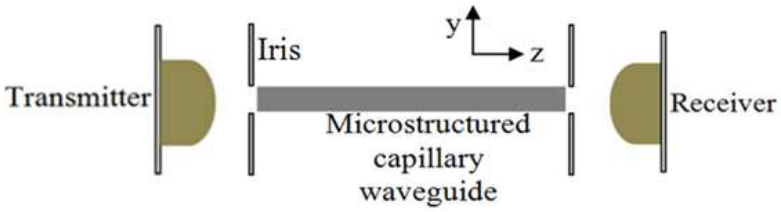

Figure 3- 2: Schematic of the experimental geometry. A 500 µm size circular aperture and iris are attached to the front and the back of the capillary to remove the unguided radiation.

The waveguide characterisation geometry is shown in figure 3-2. The waveguides ends were polished flat and studied using time domain (TD) imaging using positionable fibre-coupled 10 µm-dipole receiver. A plane wave with electric field along the x-axis (E_x) and a large input diameter of ~6mm was launched to excite the fundamental mode. Iris was fixed to the front and the back of capillary to remove unguided radiation. Using a motorized translation stage, the receiver assembly may scan across of the output end of the capillary waveguides to the map transmitted field.

The hollow core microstructured waveguides were fabricated in three different designs as shown in figure 3-3 to compare the bandwidth, dispersion and spatial confinement. All consisted of a thick silica capillary jacket containing smaller capillaries arranged around a core without a central supporting capillary. The structured was drawn down from a preform by stacked tubes to the aid of a controlled pressure of nitrogen in the central core to prevent the tubes from collapsing.

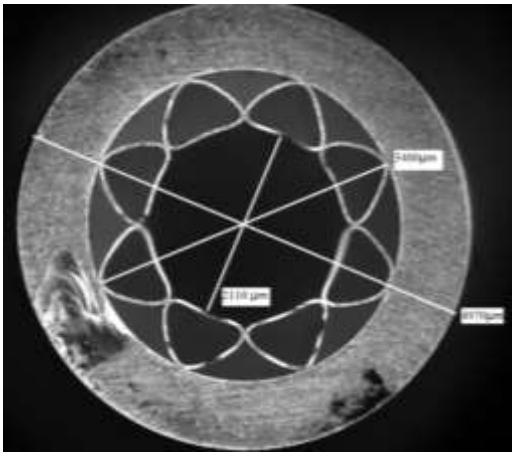

(a)

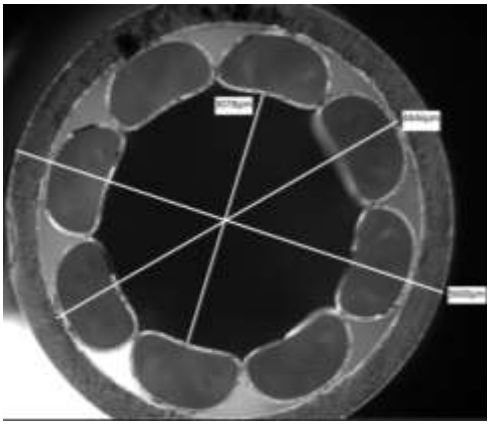

(b)

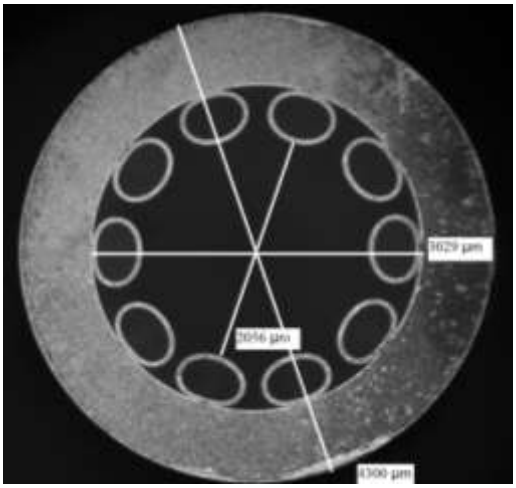

(c)

Figure 3- 3: Photograph of transverse cross-section of the capillary with inner diameter D, and a thin ring cladding with wall thickness t. The length of a sample (a) is 20.7 cm as a sample A (b) 14.9 cm as a sample B and sample (c) is 13.6 cm as a sample.

Figure 3-4 (a) and (b) show the time domain signals of the three waveguides

A, B and C. The signal was obtained in the setup shown in Figure 3-2 . The

time domain signal exhibit initial fast oscillation which indicate that the guided under exhibit a negative dispersion (higher frequency components comes first). The occurrence of THz signal pulse encounter significant reshaping and broadening during the waveguide transmission and transpire strongly frequency chirped.

The corresponding spectra of the time domain traces are plotted in Figures 3-4 d, e, and f. For sample A, a clear dip of frequency resonant showed at 1.75 THz and 2.3 THz, for sample B, the frequency resonant showed at 1.15 THz, 1.25 THz and 1.7 THz and for the sample C the frequency resonant showed at 1.9 THz which shows a good agreement with the calculation of Eq 3.8. It is noticeable additional loss appears below 0.8 THz for sample A, below 0.55 THz for sample B and 0.7 THz for sample C. Below these frequencies the guiding break down because of reduced reflections of the core walls at long waveguide which is angle of incidence increase with wavelength. The mode could be recognized as the frequency components between the dip frequency and the first resonant frequency. This implies that in the low frequency components there is no guiding in the wall, light leave the fibre is through the outer jacket. The transmission window is widened in the capillary tube with larger core diameter. This transmission for both fibers arrive almost at the same time as the reference for all frequencies, i.e. there is little group delay in the modes that are guided in the core of these capillary waveguide [11] .

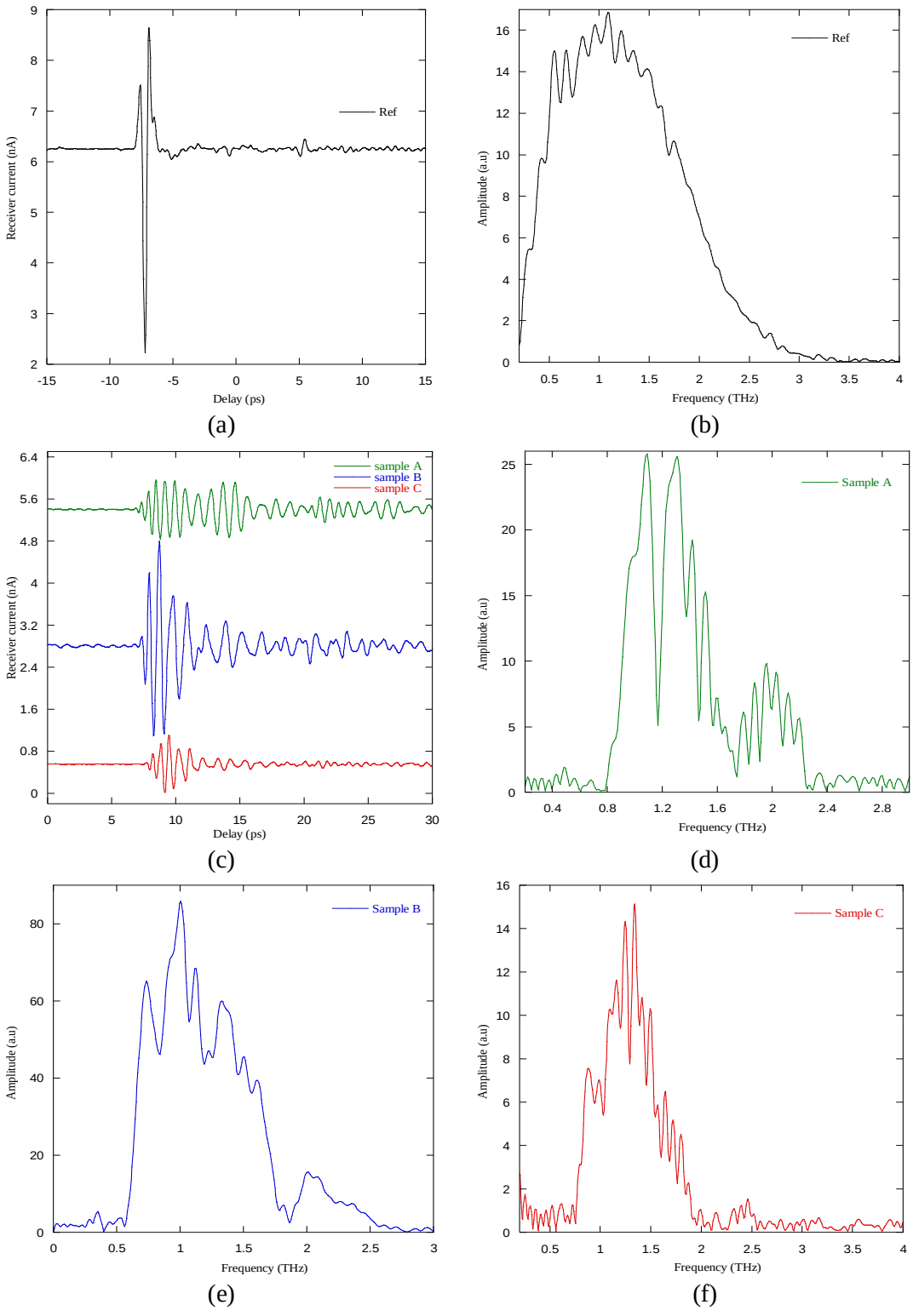

Figure 3- 4: (a) Time domain traces as a reference without a sample. (b) Corresponding FFT of time domain traces for reference (c) time domain traces for microstructured capillary waveguide for a different design known as Sample A, Sample B, Sample C. (d), (e), and (f) are corresponding FFT of time domain traces for each waveguide sample A, B, and C.

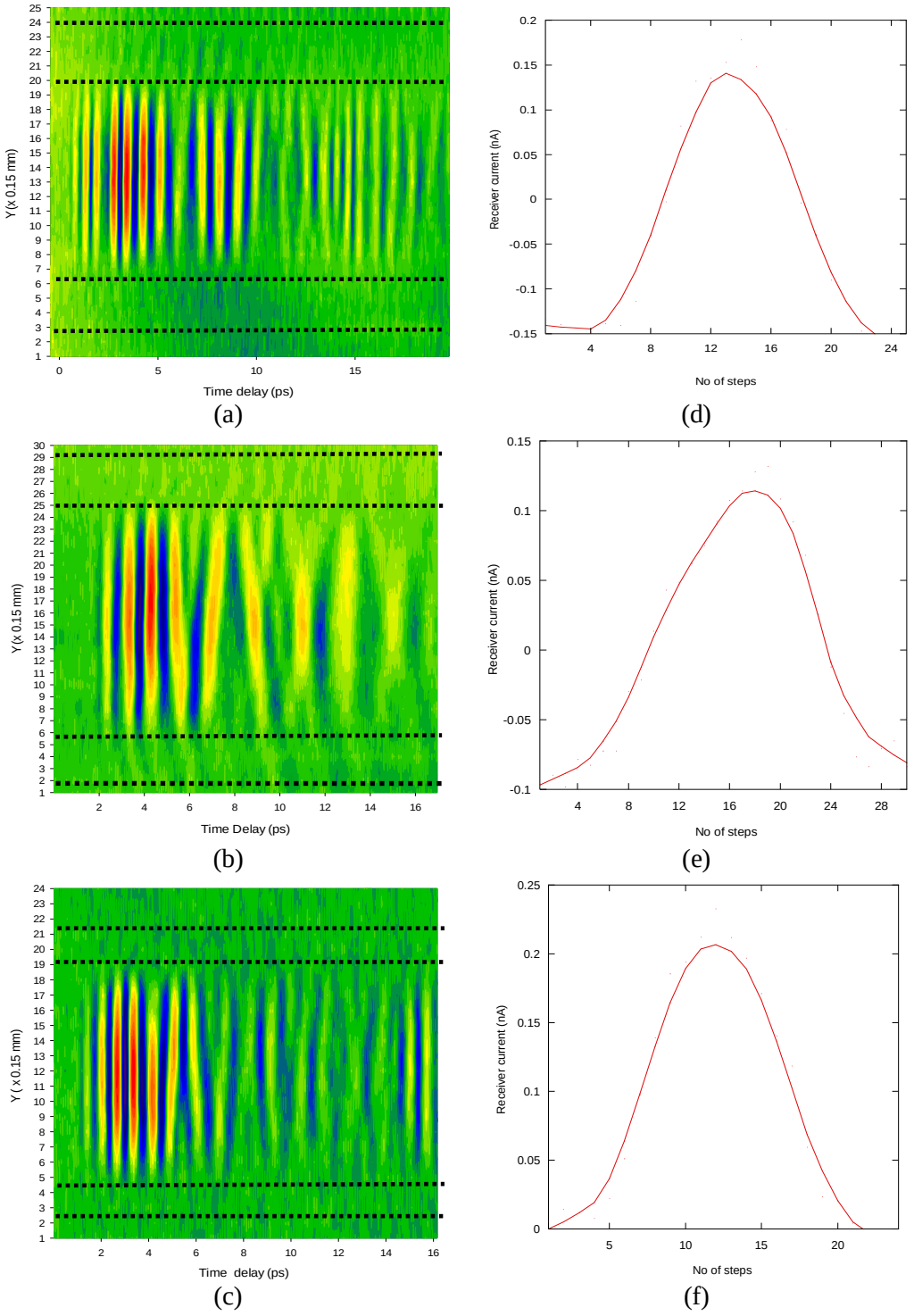

Figure 3- 5: Panels (a), (b), (c) shows space time field maps with the receiver aperture and for waveguide design A, B, C respectively with the increment of 0.15 mm. Panel (d), (e), (f) show the corresponding peak to peak amplitude at 8.75 ps. The black dashed lines indicate the position of the inner diameter of core and cladding silica wall.

Figured 3-5 shows a measurements of the beam profiles at the output of A, B and C. For all the sample, there is no clear spatial interference pattern over 15 ps which suggest that the signal contains only the HE_{11} mode. Cladding modes is not seen in the measurements.

3.4 Transmission Loss

For a hollow cylindrical waveguide surrounded by an infinite dielectric, the attenuation constant of the HE_{nm} mode is given by [13]:

$$\alpha_{nm} = \left(\frac{u_{nm}}{\pi}\right)^2 \frac{\lambda^2}{d^3} \frac{v^2+1}{\sqrt{v^2-1}} \tag{3.11}$$

where d is the diameter of the core tube waveguide and $v = \sqrt{\epsilon/\epsilon_0}$ is the complex refractive index of the dielectric. u_{nm} is the m-th root of the Bessl function $J_{n-1}(u_{nm}) = 0$. The loss is proportional to $\frac{\lambda^2}{d^3}$ but for simple capillaries with finite wall the loss is proportional to $\frac{\lambda^3}{d^4}$ [14] . The equation is not exactly applicable to a thin walled cylindrical waveguide but approximately indicates the dispersion properties β_{11} for the HE_{11} mode is very close to k_0 .This is the main reason the dispersion curves cannot be extracted from the time-domain measurement. All of the samples have a different size of the core diameter, it is impossible to compare the properties at a single frequency meaningfully. Instead, the measurement is just only upper limit loss. From this experiment, the upper limit loss from the microstructured capillary for sample A is 4.6 dB/m, 15.4 dB/m for sample B and 13.5 dB/m for sample C. The calculated

optimal cladding to core radius ratio (CCDR) in similar structure is 0.65 [15]. The cladding needs to have a sufficient thickness in order to minimise the attenuation through the evanescent field and to avoid that light is reflected at the core or cladding interface penetrates the cladding and reaches the outer diameter of the sample. A general rule is to keep the cladding diameter greater than 8-10 times the mode field diameter of the fundamental mode. The ratio cladding to the core of the microstructured capillary waveguides for sample A is 0.61, 0.81 for sample B and 1.0 for sample C. The ratio for sample A and B is not too far from the optimum.

The CCDR value depends on the desired wavelength application. Typically the cladding thickness is at least ten times the longest wavelength of interest. The main disadvantage of ARROW wave guiding is that loss is an order of magnitude greater than that in thin dielectric coated metal tubes. However, the losses decrease rapidly with increasing core diameter and are not a limiting feature in all applications and the single mode propagation and controllable transmission band could be useful in some applications. Transmission loss of this type of waveguide is mainly related to light leaking from the core when the condition of $\lambda \ll$ diameter is not satisfied. At the frequencies used have, this is not really the case.

3.5 Microstructured Waveguide Imaging using Photoconductive near field probe.

Diffraction limits the spatial resolution for conventional THz spectroscopy to a few hundred micrometers. In order to overcome this limitation, two techniques that can be used which are electro-optic sampling with a focused probe beam and photoconductive detection with an integrated aperture. In these examples, the probe beam or aperture size determines the ultimate spatial resolutions. The probe used to study waveguide as discussed in chapter 2. It consists of a 10 μm dipole antenna on LT-GaAs placed 2 μm behind a 20 μm square Al aperture and mounted on a motorized xyz stage. The probe system frequency response is centered at 1 THz with a 10% amplitude bandwidth of 2.5 THz.

The near-field probe was used to measure the temporal and frequency waveform in the plane of the output face of the waveguide shown in figure 3-6. At the beginning of the biased window, the majority of the power is confined in the inner waveguide core. The electric field is non-zero in the cladding because of the weak guiding. The minimum of the electric field should be just at the inner interface of the wall because of the large core diameter which prevents the field from leaking. Figure 3-6 (b), and (c) shows the measured modal amplitude distribution for the core mode. The lower frequency modes are confined in the core. The cladding mode can be seen at a lower frequency in the measurement of spatial frequency mapping for sample A as shown in figure 3-6 (b) since the distance between the core and cladding is only ~0.63 mm.

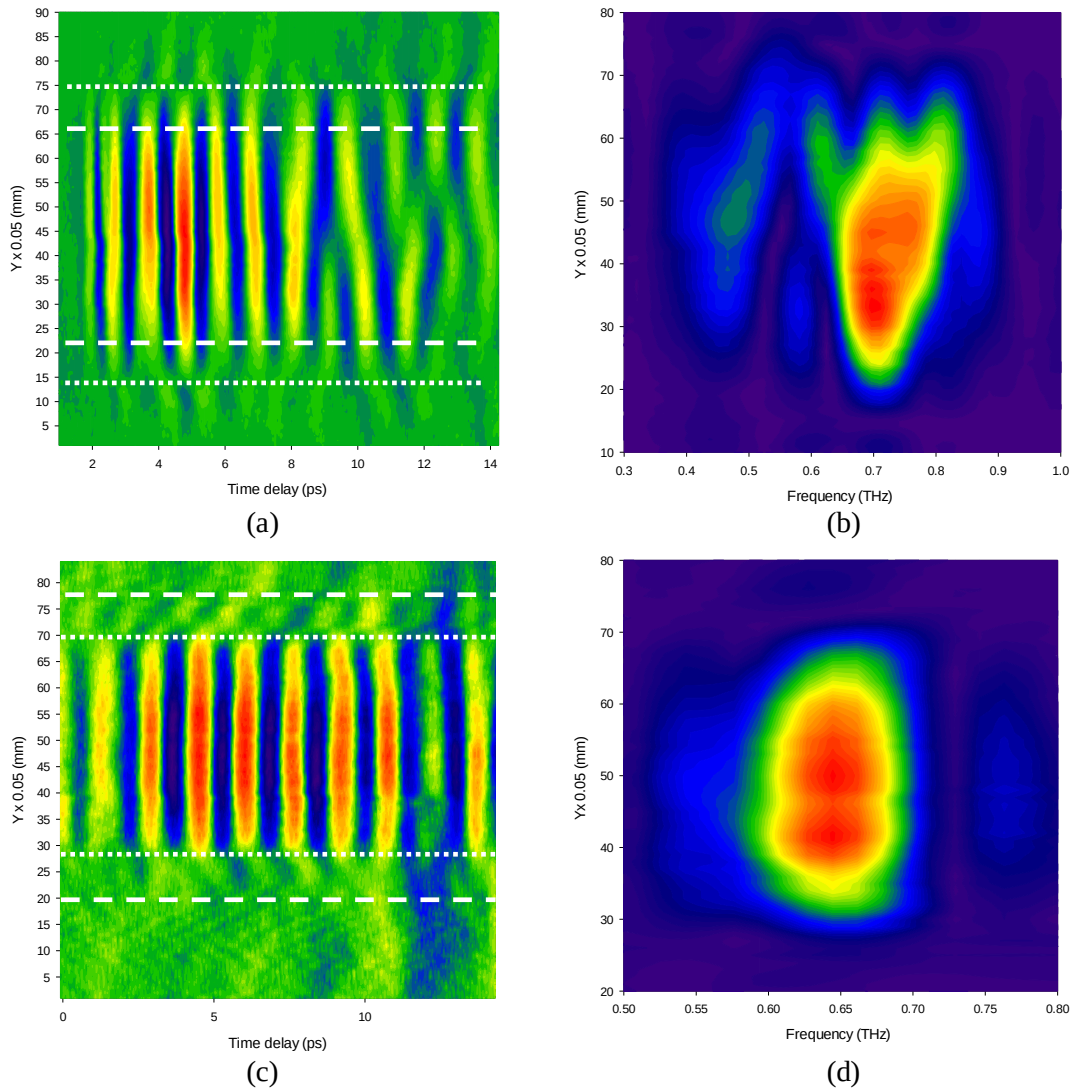

Figure 3- 6: Image of the spatial time (a) sample a, (c) sample C and frequency field mapping (b) sample A and (d) sample C for two different waveguide tube capillary waveguide obtained from the near-field probe experiment set up. The dashed line showed the position of the inner diameter core and cladding.

3.6 Conclusions

The THz guiding properties of three different design of silica microstructured capillary have been studied. The outer jacket should have a

reasonable thickness to improve the handling and makes it less fragile. The inner diameter of the waveguide need to be large as large as possible for guiding even 2 mm core does not allow flexibility. Better guiding can be achieved with having a large core diameter and small wall thickness so THz guides in silica can be flexible. Suitable polymers need to be chosen for flexibility but even there are still because of large dimensions required. Hollow core dielectric waveguides with core diameters larger than the wavelength do not generally support guiding by total internal reflection and there are no true guided modes.

This microstructured capillary waveguide design shows a different propagation transmission and bandwidth by varying the wall thickness. These features, together with the relatively high optical damage threshold of silica are attractive for prospective applications involving high optical and THz peak powers in rigid gas filled waveguides. Thick walled tube with wavelength scale core diameter can be used to reducing material attenuation and dispersion. The transmission bandwidth can be improved by reducing the cladding thickness and increasing the core size of diameter of the tube.

3.7 Reference

1. A.I. McIntosh, B.Y., S.M. Goldup, M.Watkinson and R.SDonnan, *Terahertz Spectroscopy: A Powerful New Tool For The Chemical Sciences?* Chemical Society Reviews, 2012. **41**: p. 2072-2082.

2. Grischkowsky, R.M.a.D., *Plastic Ribbon THz Waveguides.* Applied Physics 2000. **88**: p. 4449-4451.

3. H.Han, H.P., M.Cho and J.Kim, *Terahertz pulse propagation in aplastic photonic crystal fiber.* Applied Physics Letters, 2002. **80**: p. 2634-2636.

4. J.Y.Lu, C.P.Y., H.C.Chang, H.W.Chen,Y.T. Li, C.L. Pan, C.K.Sun, *Terahertz air-core microstructure fiber.* Applied physics Letters, 2008. **92**: p. 064105.

5. Shaghik Atakaramians, 3,* Shahraam Afshar V.,2 Tanya M. Monro,2 and Derek Abbott3, *Terahertz dielectric waveguides.* Advances in Optics and photonics, 2013. **5**: p. 169-215.

6. Pan, Y.a.A., S. R., *Terahertz waveguiding between parallel dielectric films.*Optics Express, 2015. **23**(1): p. 274-281.

7. Cavour Yeh, F.S., and Peter H. Siegel, *Low-loss terahertz ribbon waveguides.*Optical Society of America, 2005. **44**(28).

8. Andrews, S.R., *Microstructured terahertz waveguides.* Journal of Physics D:Applied Physics, 2014. **47**: p. 1-19.

9. Yi.Pan, *Terahertz time-domain spectroscopy and near-field imaging of microstructured waveguides*, in *Physics*. 2013, Univeristy of Bath: University of Bath. p. 108.

10. Chih-Hsien Lai, B.Y., , Ja-Yu Lu, and B.Y. Chih-Hsien Lai, Ja-Yu Lu, Tze-An Liu, , Jin-Long Peng,Chi-Kuang Sun,Hung-chun Chang, *Modal characteristics of antiresonant reflecting pipe waveguides for terahertz waveguiding* OPTICS EXPRESS 2010: p. 309.

11. Anthony, J., et al., *THz propagation in kagome hollow-core microstructured fibers.* Opt Express, 2011. **19**(19): p. 18470-8.

12. D. Chen, M.-L.V.T.a.H.Y.T., *Optical properties of photonic crystal fibers with a fiber core of arrays of subwavelength circular air holes: Birefringence and dispersion.* Progress In Electromagnetics Research, 2010. **105**: p. 193-212.

13. Pan, Y., *Terahertz Time-Domain Spectroscopy and Near-Field Imaging of Microstructured Waveguides*, in *Physics*. 2013, University of Bath: Bath. p. 88.

14. Miyagi, M., *Bending losses in hollow and dielectric tube leaky waveguides.*Applied optics, 1981. **20**(7): p. 1221-1229.

15 .E. A. J. Marcatili, R.A.S., *Hollow Metallic and Dielectric Waveguides forLong Distance Optical Transmission and Lasers*, B.L.T. Journal, Editor. 1964. p. 1783-1800.

List of figures:

List of table:

CHAPTER 4

Planar structured metallic waveguide

4.1 Surface Plasmon Polaritons (SPPs)

Metals exhibits high conductivity at THz frequencies and metal waveguides can efficiently guide THz radiation and be coupled to using simple quasi-optical techniques [2]. As the metallic surface is nearly a perfect reflector for THz radiation, a parallel plate structure supports propagating waves with low loss and dispersion. Electromagnetic surface waves have also been explored as an alternative route to sub wavelength scale THz guiding. Recently, research at Terahertz frequencies showed the result of the propagating of electromagnetic waves of the interface between metal and dielectric giving significant interest surface Plasmon (SP) are electromagnetic waves coupled to the collective oscillation of the surface free charges at the interface between conductor and dielectric [3]. Strong localization can create a better local field enhancements from the opposite sign permittivity, ε of the metals and the surrounding of non-conducting media. The result momentum of the SP mode, $\hbar k_{sp}$ from the interaction between the surface charge density and electromagnetic field, being greater than that of a free space of the same frequency, $\hbar k_0$, where the free space wave vector is

$$k_0 = {}^{\omega}/_{c} \tag{4.1}$$

So the frequency-dependent SP wave vectork_{sp}, on a flat interface separating a dielectric from a conductor is;

$$k_{sp} = k_0 \sqrt{\frac{\varepsilon_d \varepsilon_m}{\varepsilon_d + \varepsilon_m}} \tag{4.2}$$

where ε_m, is frequency-dependent permittivity of the metal and ε_d, is dielectric material. This condition may achieved with metal because of the permittivity of metal is both negative and complex [4]. Other result of SP activity along the surface is the field perpendicular to the surface decays exponentially with distance from the surface which prevents the power from propagating away from the surface.

The propagation of surface plasmon will gradually attenuate because of the losses from absorption in the metal which depends on the dielectric function of the metal at the oscillation frequency of the surface plasmon. The propagation length is;

$$\delta_{sp} = \frac{1}{2k_{sp}^{''}} = \frac{c}{\omega}\left(\frac{\varepsilon_m' + \varepsilon_d}{\varepsilon_m' \varepsilon_d}\right)^{\frac{3}{2}} \frac{(\varepsilon_m')^2}{\varepsilon_m''} \tag{4.3}$$

where $k_{sp}^{''}$ is imaginary part of complex surface plasmon wavevector, $k_{sp} = k_{sp}'+ik_{sp}^{''}$, ε_m' and ε_m'' are the real and imaginary of the dielectric function which $\varepsilon_m = \varepsilon_m' + i\varepsilon_m''$. Usually, silver (Ag) was used as a metal media because of the range of the propagation distance is 10-100 µm [6]. The activity of SP can be categorized as a surface plasmon polaritons (SPPs) which are the propagating of surface plasmon supported by planar interfaces whereas, the dimension of particle plasmon is smaller than the wavelength of the exciting radiation. The

important characteristic of the SP, is the sensitivity to the frequency index of the dielectric media giving an open route of better establishments in sensing application [2].

The characteristics of surface plasmon polaritons (SPPs) are determined by the complex permittivity of conductors at Terahertz frequency as described by Drude model. The value of permittivity of metals leads to weaker confinement compared to semiconductor and reduces the penetration of the electromagnetic field into the metal and minimizing its coupling to free charges and ohmic losses are reduced. A major approaches correspond to the Sommerfeld-Zenneck [7] have been employed at THz frequencies which, the electromagnetic waves bonded to metal surfaces are obtained by perforating these surfaces with periodic arrays of holes or excited on semiconductor surfaces.

SPPs electromagnetic waves are coupled to the free charge carriers at the interface separating a conductor from a dielectric. This coupling leads to longitudinal surface charge density oscillations, polarized along the propagation direction of the surface and the amplitude fields decay evanescently away from the interface.

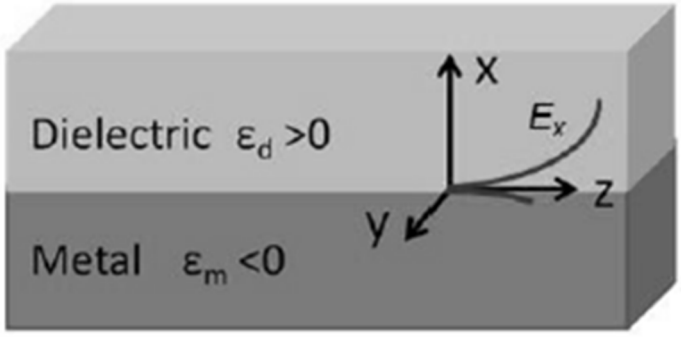

Figure 4- 1:Geometry for surface plasmon polariton propagation at a single interface between a metal and a dielectric. The large extent of the field penetration into the dielectric and the small penetration into the metal are indicated [1].

Figure 4-1 above shows the surface plasmon polariton (SPP) is a coupled excitation of an electromagnetic wave and the electron plasma at the interface of a metal and dielectric [4]. This basic simple geometry of SPPs is single flat interface between a dielectric and metallic as a conducting media which can be achieved at frequencies below the bulk plasmon frequency, ω_p.

The frequency of the SPPs approaches the characteristic surface plasmon frequency as showed in Figure 4-2. The surface charges can generate collective oscillation and SPPs can be excited. The dielectric function of a bulk metal can be well described by the Drude model; ε_m has the free electron form

$$\varepsilon_m = 1 - \frac{\omega_p^2}{\omega^2} \tag{4.4}$$

where, ω_p is the frequency of bulk plasma oscillations. The SPP frequency is given by

$$\omega_p^2 = \frac{Ne^2}{m_e \varepsilon_0} \tag{4.5}$$

where N is the free electron density per unit and m_e is the effective electron mas. The surface plasmon frequency is

$$\omega_{spp} = \frac{\omega_p}{\sqrt{1 + \varepsilon_d}} \tag{4.6}$$

where ε_d is a dielectric constant. From the equation 4.1 and 4.2 it can be seen that the SPP frequency is lower than the bulk plasma frequency [5].

At low frequency, the damping term in eq. 4.8 can be neglected and the dielectric constant becomes,

$$\varepsilon_m = 1 - \frac{\omega_p^2}{\omega^2} \tag{4.7}$$

The surface plasmon dispersion is related to the permittivity by [4],

$$k_z = \frac{\omega}{c} \sqrt{\frac{\varepsilon_m \varepsilon_d}{\varepsilon_m + \varepsilon_d}} \tag{4.8}$$

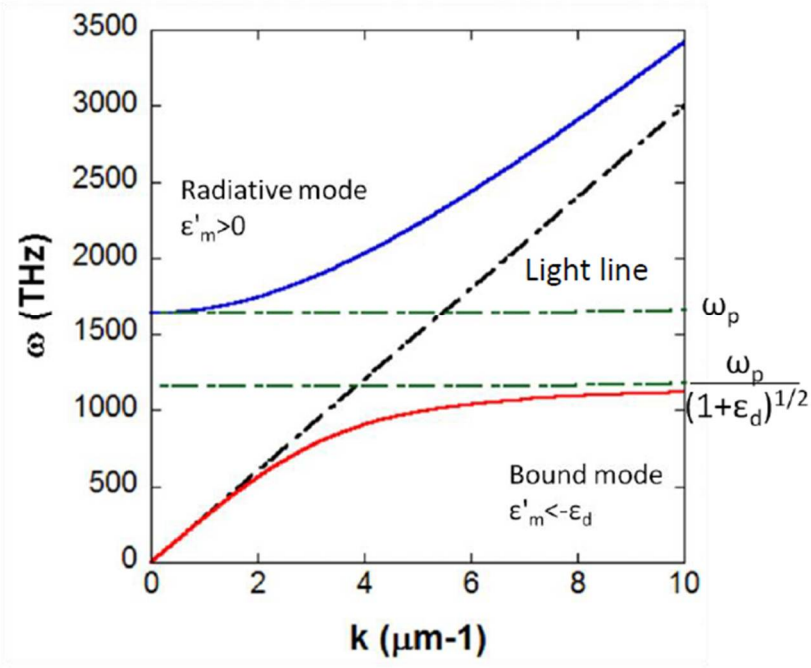

Figure 4- 2:Dispersion curve of a SPP wave on air-copper interface. The black dash line is the light line. N is 8.48 x 1028 m-3 [1].

Figure 4.2 showed an example of the dispersion curve for SPP at an air-copper interface. The red curve represents the surface plasmon dispersion which lies below the light line and bound to the surface and the blue curve is leaky and unbound.

The electromagnetic fields for both dielectric and metal, decay exponentially along the x-axis for the bound SPP mode [6]. The decay length L_x is the distance over which the electric field of the SPP is reduced by a factor of $1/e$,

$$L_x = \frac{1}{Im(k_x)} \tag{4.9}$$

$$k_x = i\sqrt{k_0^2 - k_z^2} \tag{4.10}$$

With$\varepsilon_m \ll -\varepsilon_d$, the decay lengths can be approximated by

$$L_x = \frac{c}{\omega}\cdot\begin{cases} 1/\sqrt{|\varepsilon_m|} \\ \sqrt{|\varepsilon_m|/\varepsilon_d^2} \end{cases} \qquad \begin{matrix} in\ metal \\ in\ dielectric \end{matrix} \tag{4.11}$$

Where $Im(\varepsilon_m) \sim \sigma/\omega\varepsilon_0$ and the skin depth is typically < 100 nm at 1 THz and the decay length in metal can also be estimated from the sin depth at low frequency,

$$\delta_s = \sqrt{\frac{2}{\omega\mu\sigma}} \tag{4.12}$$

SPP is also known as a Zenneck wave [7] on a flat metal surface and in order to further localize the surface mode, the used of dielectric with higher constant material like a thin dielectric coated onto the metal surface can be used in order to improve the localization of surface mode and to enhance the dispersion and material absorption [1].

4.2 Spoof Surface Plasmon Polaritons (SSPPs)

Spoof plasmon is electromagnetic surface waves with designer dispersion mimicking (SPPs). This is because these waves allow for sub-wavelength

confinement of the field and allow modifying the systems to miniaturization. So in this case, the study of the characteristic propagation of the wave between the interfaces is very interesting along with the geometrical structures resulting the optimal guiding and localization of THz energy [8]. Any disturbance of a flat surface can bind a surface mode as reported by Ulrich [9], THz guiding on a planar metallic mesh.

Earlier work suggested that sub wavelength scale structuring of a metal surface can be used to engineered the dispersion of surface waves and periodic metallic structures can guide tightly bound THz surface waves which have similarities to the much higher frequencies. Although, SPPs are weakly bounded to the metal-dielectric, because of the metal behavior near the perfect electric conductor (PEC), spoof surface plasmon polaritons can be achieved by the introduction of one or two dimensional surface configurations or periodic textures on metal surfaces and excited on a periodically structured of perfect electric conductor (PEC) surface. It's mimicking the activity to imitate the electromagnetic of surface plasmon polaritons for example focusing, guiding, and localization [10].

An effective plasmon frequency is determined by the hole dimension, a, which is an infinitely deep square hole of a periodic hole array of metal on flat sheet [11] , rather than metal properties and can be shifted below ω_c by filling the holes with dielectric. An effective “plasmon” frequency is determined by the hole dimension,

$$\omega_{pl} = {}^{\pi c}/_{a\sqrt{\varepsilon_h}} \qquad (4.13)$$

with ε_h, is the permittivity of the dielectric material filling the holes and the in plane dispersion, where *d*, is the period is obtained as,

$$k_z^2 c^2 = \omega^2 + \frac{1}{\omega_{pl}^2 - \omega^2} \frac{64 a^4 \omega^4}{\pi^4 d^4} \tag{4.14}$$

Diffraction at the first Brillouin zone boundary give cut off frequency as,

$$\omega_c = \frac{\pi c}{d} \tag{4.15}$$

which is lower than the spoof SPPs frequency, ω_{pl} if $\varepsilon_h = \varepsilon_0 \, . \, \omega_{pl}$ can be shifted below ω_c by filling the holes with dielectric[12] for example wax was used in this study. ω_{pl} is determined by the geometry rather than the properties of the metal. Therefore, SSPPs pioneered such studies with works on square holes arrays [13] and annular holes [14].

If the conductor is a perfect material without loss, the spoof plasmon is a promising tool for the concentration of THz radiation because of the possibility of focusing with the periodically holes array and therefore spoof SPPs offer another solution to confining guided modes at surfaces.

4.3 Normal Transmission

The transmission is strongly attenuated at frequencies below the cut-off frequency with domination of TE_{11} mode contribution for circular holes. The periodic hole arrays acts as a grating to coherently scatter incident radiation

into SSPPs. The resonant scattering wave vector for the SSPP mode are given by [15],

$$k_{sspp} = k_z \pm G_{i,j} = k_0 \sin\theta \pm i\bar{b}_1 \pm i\bar{b}_2 \tag{4.16}$$

where $k_z = k_0 \sin\theta$ is the in-plane component of the incident wave vector, θ is the incident angle, i and j are the integers. If the real space primitive vectors $\bar{a}_1 = \frac{g\bar{x}}{2} + \sqrt{3}g\bar{y}/2$ and $\bar{a}_2 = g\bar{x}$, the reciprocal lattices are $\bar{b}_1 = 4\pi\bar{k}_y + \sqrt{3}g$ and $\bar{b}_2 = 2\pi(\sqrt{3}\bar{k}_x - \bar{k}_y)/\sqrt{3}g$ for the hexagonal hole array of the sample in this study, where g is the pitch of the hexagonal hole array. For normal transmission, the resonant wavelengths are given by [16],

$$\lambda = \frac{g}{\sqrt{\frac{4}{3}(i^2 + j^2 + ij)}}\left(\frac{\epsilon_d \epsilon_m}{\epsilon_d \epsilon_m}\right)^{1/2} \tag{4.17}$$

Diffraction on periodic arrays also gives rise to spectral minima known as Wood or Raleigh anomalies. At normal incidence, the wavelength of Wood anomalies is given by [16],

$$\lambda_R = \frac{\sqrt{3}g}{2n} \tag{4.18}$$

where $n = \pm 1, \pm 2 \ldots$ .At Thz frequencies, λ_R is almost equal to the SSPP wavelength because $\epsilon_m \ll -\epsilon_d$.

4.4 Periodically Perforated Metal Film

A periodically perforated metal films is be used as a planar spoof plasmonic THz wave guiding devices. With THz spoof surface plasmon dispersion on periodic meal structures and the guiding mode can be explored over a broad spectrum.

The samples used have the hexagonal lattices with a pitch of g, and thickness of, t. Each hole has a diameter of d_t, on the top side which tapers to a minimum diameter of d_b, on the bottom side. In this experiment, a periodically perforated metal film with hexagonal arrays of sub wavelength size circular holes as in figure 4.3 were used to explore a wave guiding on two surfaces. The samples were made using electroforming techniques on the nickel sheet and sold under the commercial name of Hi Mesh. In a previous study, perforated metal screens have been used as a far-infrared band pass filter with a transmission peak 0.9 at frequencies 1.8 – 4.2 THz[17] 337 μm electromagnetic radiation wavelength has been guided in the form of TM surface waves along thin copper sheets perforated in a regular pattern (metal mesh) [9]. In this experiment, this sample was used to study the in-plane wave guiding properties. All the dimensions are showed in table 4-1. The bottom side has a shiny flat surface with holes of a good round shape.

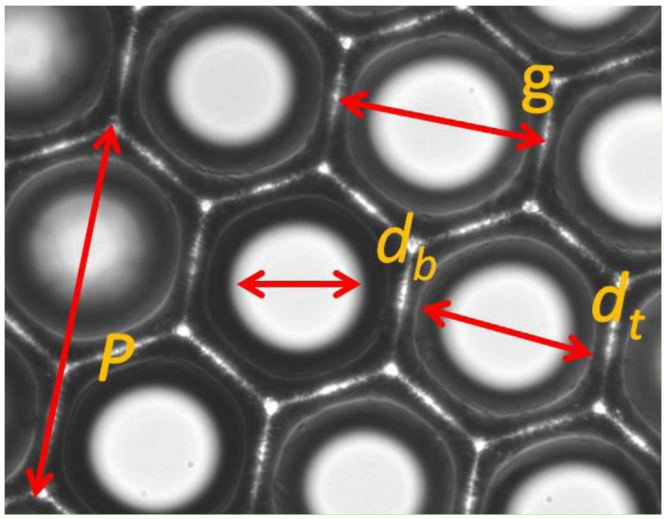

Figure 4- 3:Microscope image of the upper surface of a metallic mesh with pitch g, hole diameters, db and dt [1].

Table 4- 1:Dimension of HiMesh samples [1].

Parameters	Dimension (µm)
Pitch (g)	91±1
Upper diameter hole, $d_{t,}$	77±2
Lower hole diameter, d_b	55±2
Thickness, t	55±1

4.5 In-plane THz wave guiding on a perforated metal film

The set up shown in the figure 4.3 below was used to study the waveguide properties of Hi Mesh 275. The sample was kept flat by stretching it over two metal bars by attaching with small magnets and the edge of the mesh. Steel razors blades were placed on the both side of the sample surface with a gap of ~100 µm to minimize the signal from unguided waves.

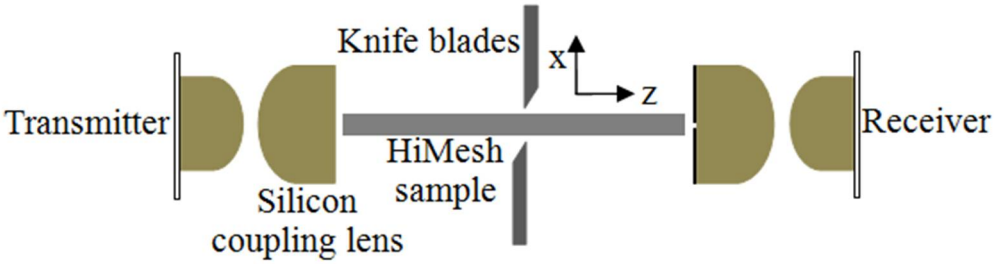

Figure 4- 4:Schematic of HiMesh experimental set up.

In the experimental setup shown in figure 4.4, a cylindrical silicon lens was used to couple in and out of the SSPP mode waveguide. The output silicon lens was placed at the end of the waveguide with 100 µm gap between the lens and the sample. A pair of Mylar films with a gold coating are placed on the collection silicon lens to create an open slit ~220 µm.

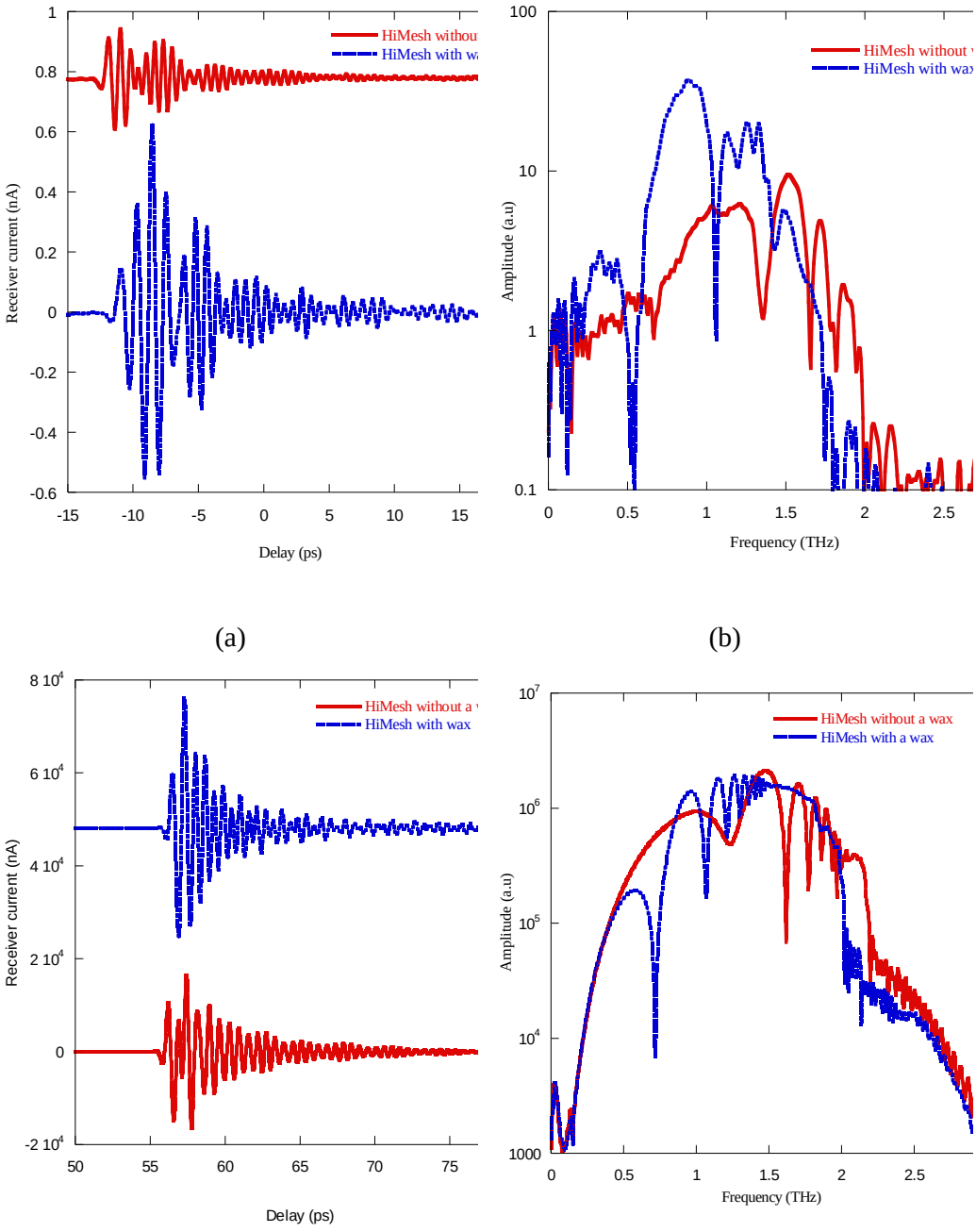

Figure 4- 5: (a) Time-domain traces for HiMesh 275 with and without wax and (b) the corresponding spectra of the traces. (c) simulated time-domain traces of the HiMesh without wax using CST microwave studio simulator (d) the corresponding frequency spectra traces with an increment of 0.05 mm.

The collection lens was translated along the x-axis and placed at the minimum signal amplitude of the waveguide which is at the edge of the waveguide (x=0). Figure 4.5 (a) and 4.5 (c) shows the time domain measurements at the x position of 0 (x=0) for the experimental and simulation correspondingly. The corresponding spectra in the figure 4.5 (b), (d) exhibit a series of sharp dips which moving closer together with increasing of frequency. The chirped spectrum arises from interference between two surface modes with different nonlinear dispersion because the nonlinear dispersions have a rapid change in phase at frequencies close to the cutoff frequency. By depositing a thin layer of wax with the index is 1.3293 within the holes and scraped of the surface so it's filled inside the hole about, its reveal the dips on the spectra become closer together at much lower frequency compare to without a wax as shown in figure 4.5 (b)(d). From the simulation of Hi Mesh using a CST microwave studio simulator figure 4.5 (c) , the spectrum corresponding of the time traces showing that an agreement between the calculation and experimental for the Hi Mesh without wax where is the dips become close together as the frequency become higher as shown in figure 4.5 (d) . For Hi Mesh with a wax, the dips exhibit at much lower frequency with calculation in simulation. A time mapping for the Hi Mesh is shown in Figure 4.6 (a), (c), and the corresponding frequency mapping is showed in figure 4.6 (b), (d). The simulation of time mapping result for HiMesh is shown in Figure 4.7 (a), (c) and the result for frequency mapping is shown in Figure 4.7 (c), (d) correspondingly. The dips shift in frequency and change amplitude along both x and z waves. The strong interference between the SSPPs occurs in the near field region$(z < \lambda)$. The lower surface has smaller diameter holes which

should support a more dispersive mode, so that the dispersion curve bends away from the light line faster than the upper surface guiding mode.

4.6 Modal interference

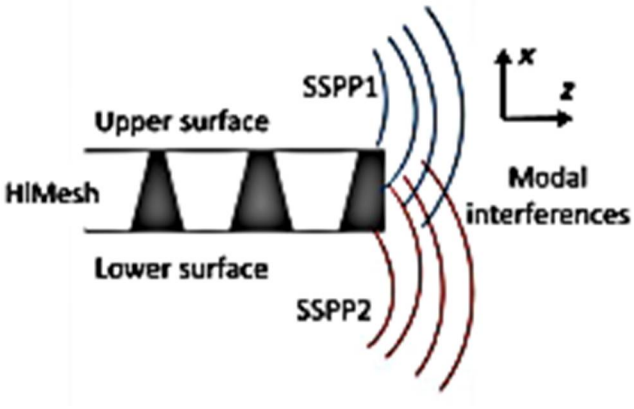

Figure 4- 6: Schematic of the SSPP modal interference for upper surface an lower surface of HiMesh 275

The HiMesh 275 sample was simulated using CST Microwave studio with nickel material conductivity of 1.44 x 10^7 S/m and surface impedance matching boundary were used. The circular holes were modelled as truncated cones with upper diameter of 55 and lower diameter of 80 µm. the thickness of the structure is 50 µm with 92 µm pitch size. The structure was modelled as a PEC consisting 40 x 20 hole array. The stimulated length was 1cm and probes were placed 160 µm away from the waveguide end. A port mode with the electric field parallel to the x axis was used to excite modes on the upper and lower surface as shown in figure 4-1 above.

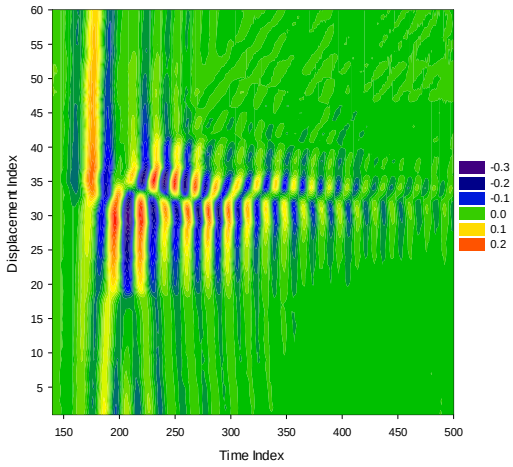

(a)

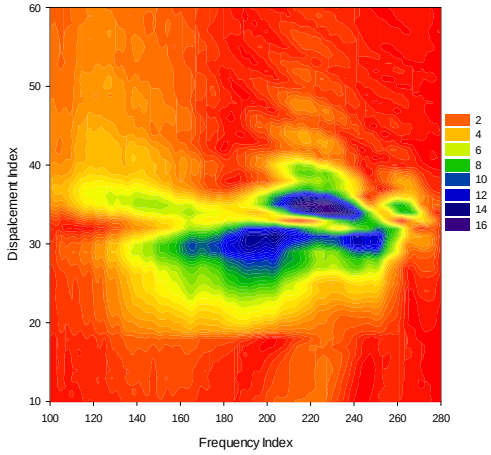

(b)

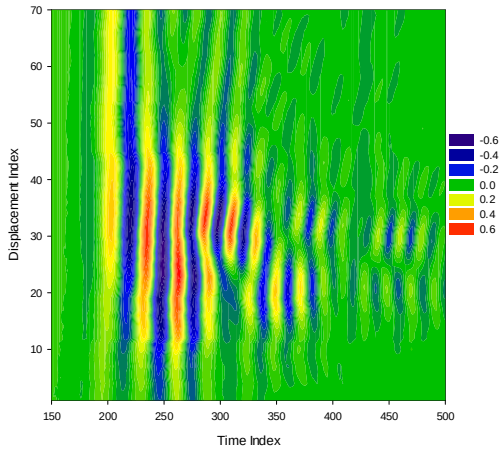

(c)

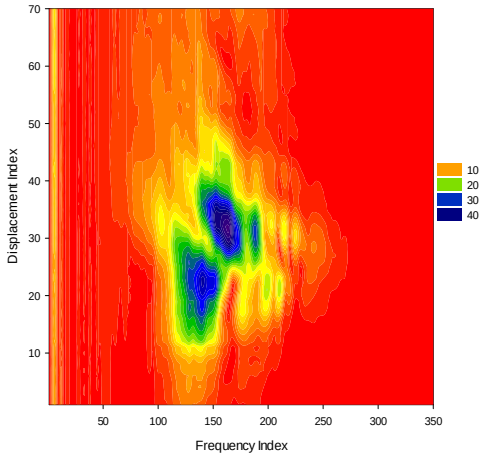

(d)

Figure 4- 7:(a) Experimental time-domain mapping for HiMesh 275 and (b) the corresponding spectra mapping of the traces (c) Time-domain mapping of the HiMesh with deposition of wax (d) the corresponding frequency mapping with the increment of 0.05mm.

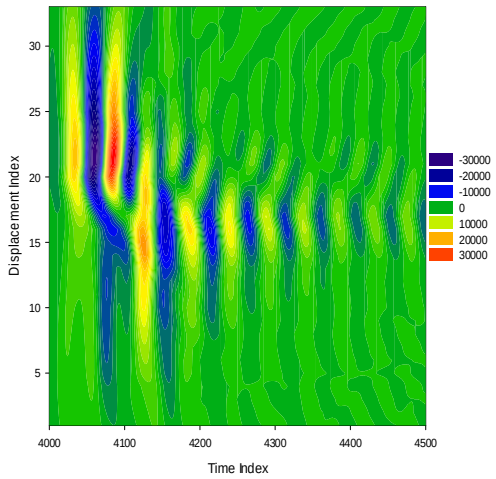

(a)

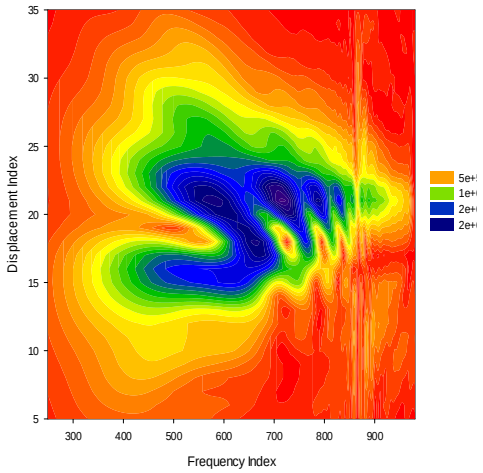

(b)

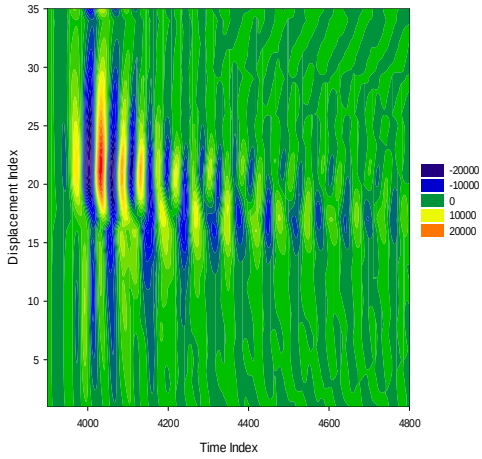

(c)

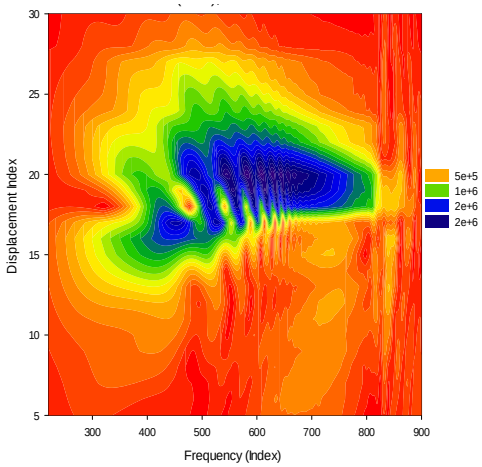

(d)

Figure 4- 8:(a) CST simulation of time-domain mapping for HiMesh 275 (b) the corresponding spectra of the traces (c) CST simulation of time mapping of the HiMesh with wax deposition (d) the corresponding frequency mapping with the increment of 0.05mm.

Because of this sample is asymmetric between the two surfaces, the lower surface with smaller diameter holes support more dispersive mode and the dispersion curve bend away from the light faster that upper surface mode and the dispersion also refractive index can be obtain by using the equation,

$$k = k_0 + \frac{\Delta\varphi(\omega)}{L} \tag{4.19}$$

where $\Delta\varphi$ (ω), is the difference between the phase spectra with and without a sample in place, L is the sample length, k is the propagation constant of the waveguide, and k_0 is the free space wave vector.

At THz frequencies, λ_R is almost equal to the SSPP wavelength because $\in m \ll -\in d$. At $\theta=0°$, the calculated Wood anomaly frequency is 2.9 THz for HiMesh 215, which corresponds to the dip at ~3 THz in Figure 2-5. Due to the THz system's spectral response, the result has poor accuracy above 2.0 THz. By normalizing to a reference value collected using the same configuration, factors that affect the signals during the task and the reference are the same. The loss of the HiMesh is due to the finite metal conductivity and scattering at imperfection. The loss would be expected to be similar in order of magnitude to other metamaterials (~ dB/cm). From previous work, Ulrich's mesh [9] have a loss of a 5dB/cm and Williams et al's dual band THz coaxial surface waveguide [18] was measured a loss of 1.91 dB/cm within a 3 THz.

4.7 Magneto-Plasmonic

Plasmonic and metamaterial structures can be function as electromagnetic wave absorbers due to the excitations of plasmonic especially in bio sensing applications [1], observed dips in the reflection of metallic absorbers with elements of periodicity with specialty designed geometries at optical frequencies. Metamaterials are artificial periodic of structured elements of sub wavelength size and smaller than the wavelength of the incident.

Planar waveguides and photonic crystals are current technologies in integrated optics to transport electromagnetic (EM) energy in structures with the dimension smaller than the wavelength of illumination [19]. A recent study showed electromagnetic energy can be transport with the optical devices with size reduction to below diffraction limit [20]. This energy is guided via an array of metal nanoparticles, with function of supporting collective electronic excitation, surface plasmon with resonance frequency depending on type and size. This metal particles exhibit strong light absorption compare to their geometrical sizes and convert the EM energy into oscillatory electron motion which is important characteristic for strong coupling into a wave guiding structures.

Previous work of Pendry [21] reported, double split ring resonator (DSSR) with nonmagnetic metallic element , with size below diffraction limit, exhibits strong magnetic response and behave as effective permeability material. At THz frequencies, SP resonances in metal nanoparticles could support resonant MP oscillation[22] and may lead the development of

metamaterial with negative indexes of refraction with combining electric response [23].

The plasmonic activity will be excited if the frequency and wave vector are matched with the propagating of the plasmon or spoof plasmon polaritons or localized surface plasmon polaritons (LSPP). A surface plasmon resonance is a surface charge density wave in a metal layer excited by light and propagating along the interface between metal-dielectric interfaces. The surface plasmon resonance (SPR) characteristic can be used as future applications especially in biosensing as a tool for label-free investigation of interactions between biomolecules [4]. The variety design of metallic particles was used to study the enhancement of local field and improve light-matter interaction.

4.8 Magnetic plasmon experimental set-up

In this study, a sub wavelength size metal structure referred as a single split ring resonator (SSRR) is used to support propagation of MP Polaritons. The application of MP for guiding EM energy has great potential for direct application in novel sub diffraction size transmission lines.

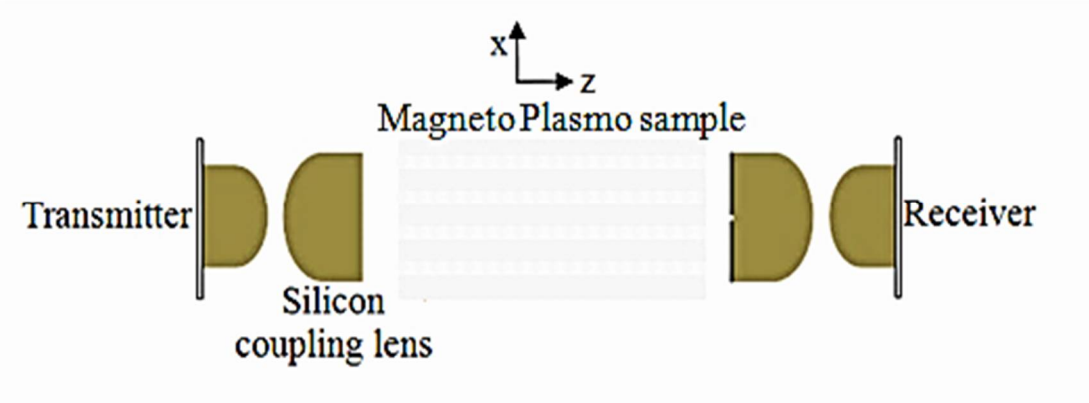

Figure 4- 9:A schematic diagram of magneto plasma experimental set up with sample thickness of mylar film is 0.036 mm

In this experiment, the experimental set up as figure 4.8 and the samples is a periodic structure on mylar film is with two different sizes of the pattern were used to explore the waveguiding transmission. A metallic material, aluminium was used as samples in order to excite plasmons. To be able to look at the differences in plasmonic excitation, four different sizes of shape and different periodicity were measured. The samples are lithographically patterned on mylar film. All samples with size dimension are shown in figure 4.9.

A design of a SRRR characterized by two metal loops with tails adjacent to their ends as shown in Figure 4-9. The different between the samples are the

size of the loops with 30µm for large pattern and 15 µm for small pattern. The gaps for symmetric pattern are 15 µm in between the loop. Excitation of magnetic response in a system of SSRRs on a planar substrate results in induction of magnetic dipoles that are perpendicular to the substrate plane. Parallel dipoles are characterized with small spatial field overlap and magneto inductive interactions between them are expected to be rather weak. Periodic structures increase coupling between the dipoles and let the conduction current flow from one SSRR to another SSRR to improve the EM energy transport along a chain of SSRRs.

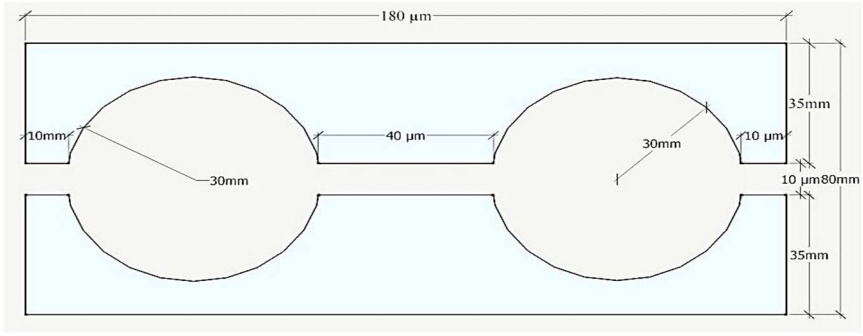

(a)

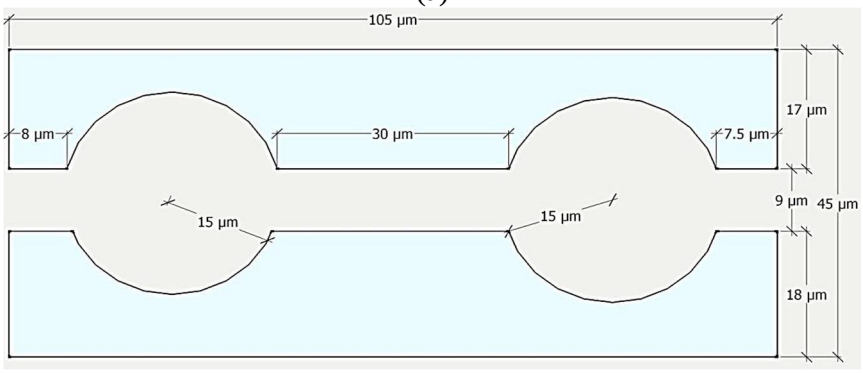

(b)

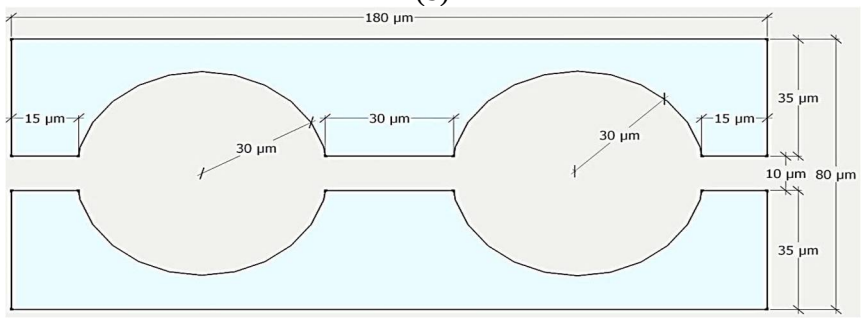

(c)

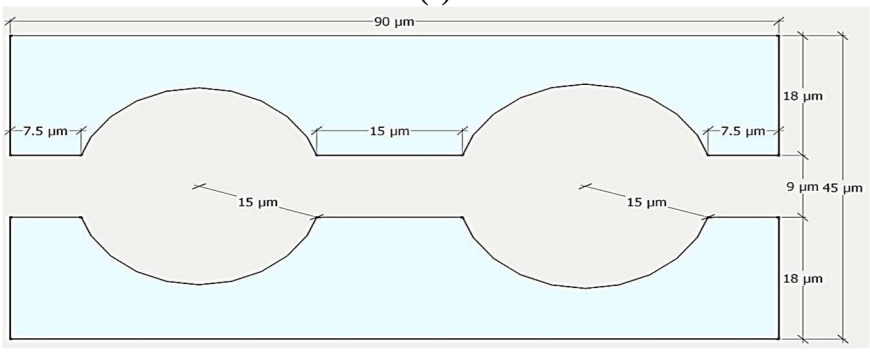

(d)

Figure 4- 10:A schematic diagram of structures of the samples on mylar fim as a substrates with (a) asymmetry large pattern (b) asymmetry small pattern (c) symmetry large pattern (d) symmetry small pattern.

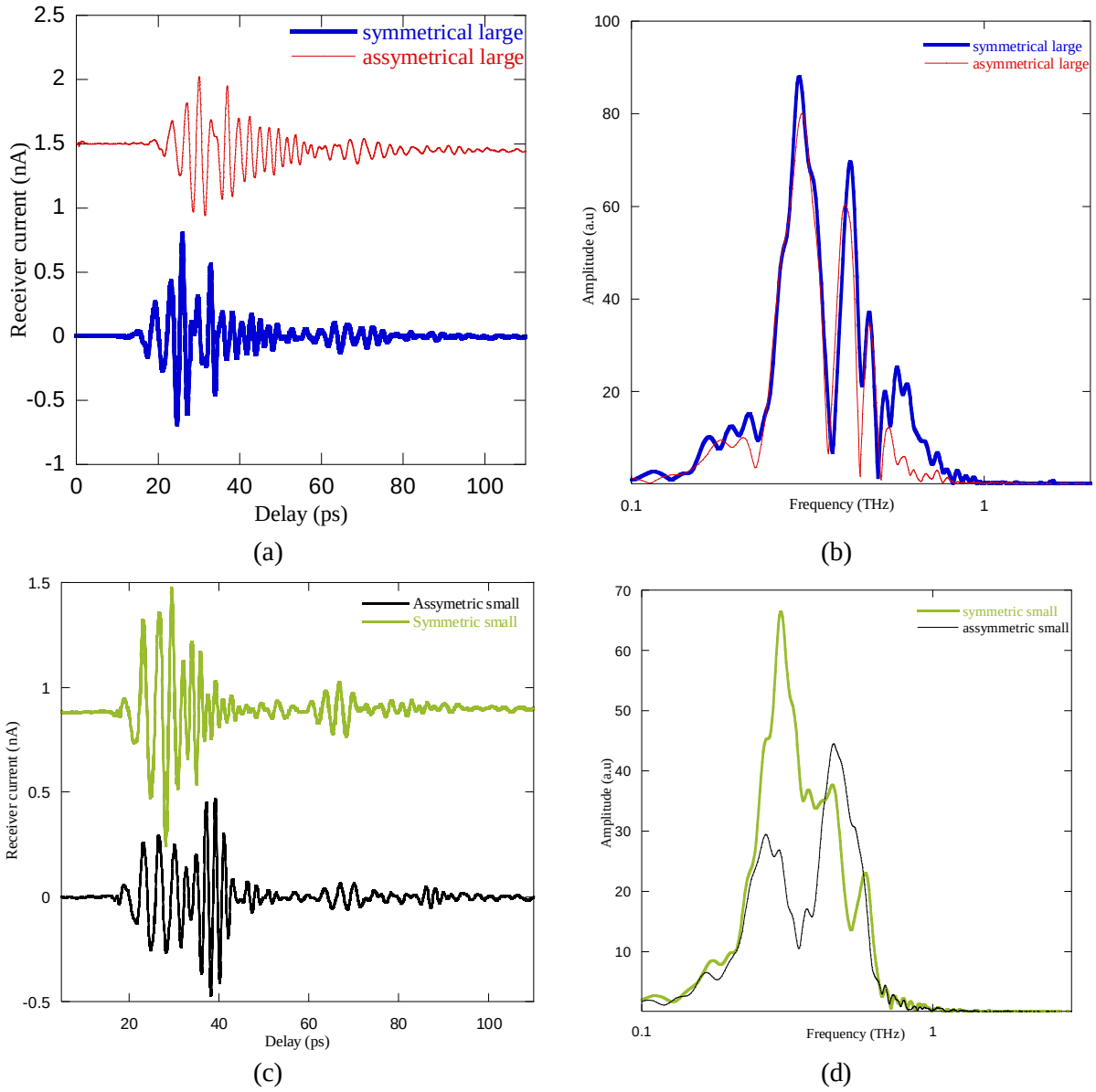

Figure 4- 11:(a) and (c) A time domain traces for assymmertical and symmertical large and small correpsondingly. (b) and (d) a FFT trace for asymmetrical and symmetrical large pattern of magneton Plasmon sample and asymmetrical and symmetrical small pattern of

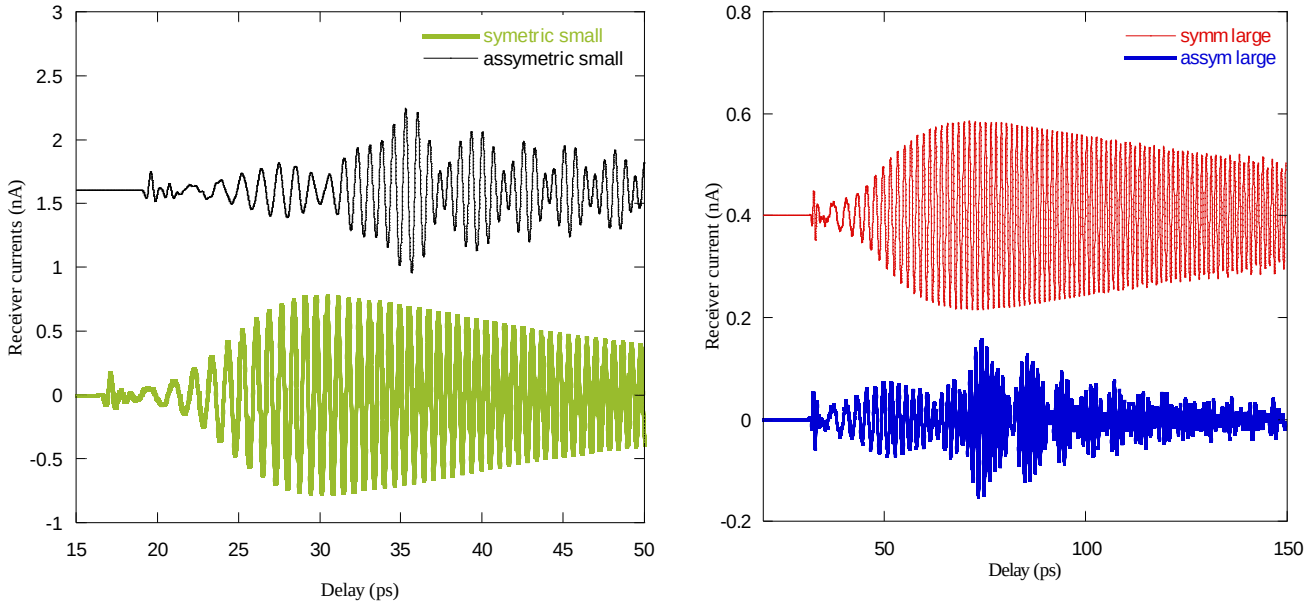

(a) (b)

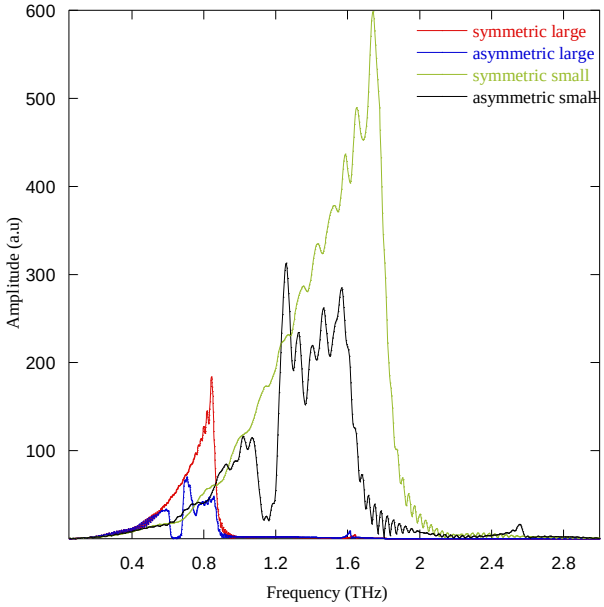

(c)

Figure 4- 12: A CST simulation of spectra of four different pattern of magneton plasmon sample known as symmetrical large, assymetrical large, symmetrical small and asymmetrical small with a 0.035mm thickness of mylar film as a substrate.

From figure 4-10, we see that spectra of a large asymmetric and symmetrical pattern showed more frequency dips compare to small pattern sample. The frequency dips for the asymmetric large pattern are clearly shown at 0.56 THz, with another sharp peak at 1.6 THz. For the asymmetric small pattern, a clear disappears at 0.3 THz. For this sample, only asymmetrical large and asymmetrical small shows a dip features on the spectrum. All of the patterns have a low broadband frequency which is 1.0 THz frequency. The contribution from symmetrical for both patterns showed more efficient signal in transmission compares to the asymmetric pattern. The smaller frequency shift could be attributed to the weaker coupling of the sample.

Figure 4-11 above shown a CST simulation frequency trace of magneto plasmon sample. Small pattern design covered broader frequency to 3.0 THz compare to large pattern design, 2.0 THz for both asymmetric and symmetrical design. The broadband frequency for a small pattern is one time bigger than the large pattern. Both large and small asymmetrical pattern show a dip features at 0.6 THz and 1.1 THz correspondingly. The experiment and theory didn’t meet agreement because of poor quality of the sample. A coupling mechanism based on exchange of conduction current could be used to improve energy transmission.

4.9 Terahertz time-domain spectroscopy to identify anomeric configuration in lactose

Lactose is formed by joining two anomer *(*which is α-D-anomer and β-D-anomer which is commonly exist in disaccharide powder and it was nondestructively and quantitatively evaluated in THz-TDS with absorption peak at 39.7 cm^{-1} (1.19 THz) for β-D-lactose and 17.1 cm^{-1} (0.53 THz) and 45.6 cm^{-1} (1.37 THz) for α-D-lactose monohydrate [24]. Previously, the anomers was analyzed by thermogravimetric analysis (TGA) and differential scanning calorimetric (DSC)[25, 26], Raman spectroscopy[27], X-ray diffraction (XRD)[28] and Fourier Transform Infrared Spectroscopy (FTIR)[29] and recently, significant characteristic between different types of biological material in pulsed THz imaging [30]. Since sugar could become of significance to THz biological detection and infrared spectroscopy is generally used to detect and analyze sugars, therefore, coupling with vibrations of entire molecules are to be predictable at terahertz frequencies[31]. Previous study showed an absorption peak of 100% lactose monohydrate powder, with 3 mm thick sample at 0.57 THz [32].

4.10 Preparation of Lactose sample

The lactose powder use for source material with a formula of $C_{12}H_{22}O_{11}H_2O$ to measure the attenuation of surface waves transmission through the lactose powder sample, these powder were mixed with a distilled water and deposited the solution uniformly on the surface of the HiMesh. The

HiMesh weight was measured before and after the deposition with electronic weight balance. The sample is left it for 24 hours until dry and is ready to use when the weight of the sample is reached 1.4 mg/10 cm^2. The schematic setup for this experiment is same like Figure 4.3.

Figure 4.12 above shows the spectra for a HiMesh 275 with and without lactose powder deposition as a reference to compare the presence of chemical substances on the surface of the HiMesh. The dips exhibit at a lower frequency with the presence of lactose powder.

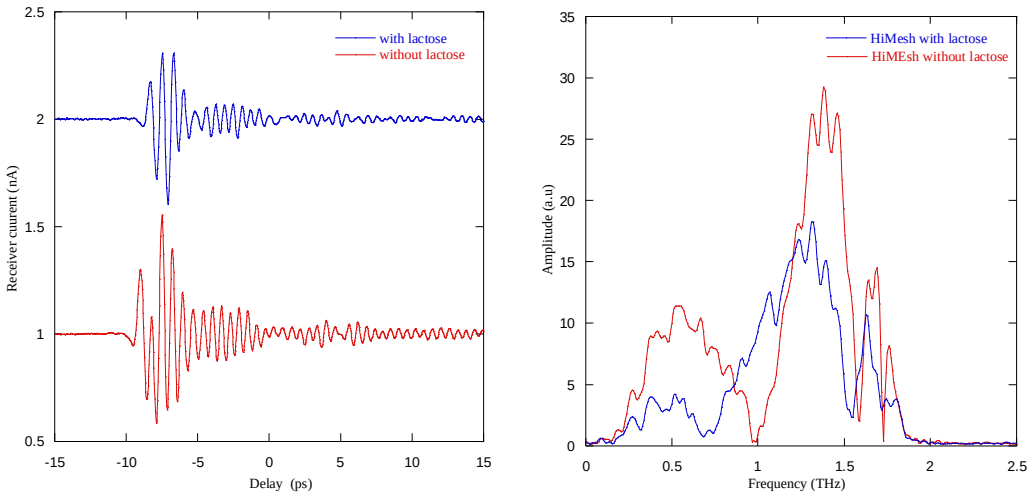

(a) *(b)*

Figure 4- 13:(a) Comparison of time domain trace and (b) the corresponding spectra of HiMesh 215 with and without lactose powder. The lactose on the square sample is 1.4mg/10cm2. (c) FFT spectra peak absorption of lactose powder.

The temporal profile of the electric field strength, represented as the induced photocurrent in the detector of the electromagnetic wave pulse transmitted through the HiMesh sample with lactose deposition and the through a HiMesh

without lactose. The sample trace is offset vertically 1nA for better visibility of the traces as shown in Figure 4-12 (a). The modification of the pulse shape due to the presence of an infrared active compound in the HiMesh sample with lactose is apparent from the difference in electric field traces. The pulse is delayed and attenuated; both are measures of the dispersion and the absorption by the sample. Figure 4-12 (c) showed the transmission spectrum. There is no clearly significant sharp dips showed at 0.57 THz but the spectrum is shifted to the lower frequency with the exhibit of the lactose powder as showed in Figure 4-12 (b).

4.11 Conclusion

In summary, we have studied the waveguide properties of freestanding nickel sheet perforated with hexagonal arrays of conical holes filled with air, wax and lactose. The HiMesh and the magneto plasmon sample may find an application in chemical sensing as the interference features are sharp and prominent over a broad frequency range. The characteristic of electromagnetic field localization and external modulation magnetic field in magneto plasmon can be used in the fields of applications of magneto-plasmonic in the domain of sensing especially in gas and bio sensing applications. Excitations of MP could be a promising for the development of a wide range of optical devices.

4.12 References:

1. Yi.Pan, *Terahertz time-domain spectroscopy and near-field imaging of microstructured waveguides,* in *Physics.* 2013, Univeristy of Bath: University of Bath. p. 108.

2. G.Gallot, S.P.J., R. W. McGowan and D. Grischkowsky, *Terahertz waveguides.* J. Opt. Soc. Am. B, 2000. **17**: p. 851-863.

3. Kawata, S., *Near-Field Optics and Surface Plasmon Polaritons.* 2001: Springer Science & Business Media. 210 pages.

4. Barnes, W.L., Dereux Alain, Ebbesen Thomas W, *Surface plasmon subwavelength optics.* Nature, 2003. **424**(6950): p. 824-830.

5. Junxi Zhang, L.Z.a.X., *Surface plasmon polaritons: physics and applications.* Journal of physics d: Applied physics, 2011. **45**(2012).

6. Pitarke, J.M., et al., *Theory of surface plasmon and surface-palsmon polaritons.* Report on Progress in Physics, 2007. **70**: p. 1-87.

7. Tae-In, J. and D. Grischkowsky, *THz Zenneck surface wave (THz surface palsmon) propagation on a metal sheet.* Applied physics Letters, 2006. **88**: p. 061113.

8. Stockman, A.R.M.D.M.I., *Theory of spoof plasmons in real metals.* Applied Physics A, 2010. **100**(2): p. 375-378.

9. Ulrich, R. and M. Tacke, *Submillimeter waveguiding on periodic metal structure.* Applied Physics Letters, 1973. **22**(5): p. 251-253.

10. Kim, A.S.-H., et al., *Waveguiding of spoof surface plasmon polaritons.* Conference on Lasers and Electro-Optics/Pacific Rim, 2015. **2**: p. 1-2.

11. Pendry, J.B., L. Martin-Moreno, and F.J. Garcia-Vidal, *Mimicking surface plasmons with structured surfaces.* Science, 2004. **305**(5685): p. 847-848.

12. A.P. Hibbins, E.H., M.J. Lockyear and J.R. Sambles, *Prism coupling to 'designer' surface plasmons.* Optics Express, 2008. **16**: p. 20441-20447.

13. C.R Williams, S.R.A., S.A Maier, A.I Fernandez-Dominguez, L.Martin-Moreno and F.J Garcia-Vidal, *Highly Confined Guiding of Terahertz Surface Plasmon Polaritons on Structured Metal Surfaces.* Nature Photonics, 2008. **2**: p. 175-179.

14. C.R Williams, M.M., S.R. Andrews, S.A Maier, S.Carretero-Palacios, S.G. Rodrigo, F. J. Garcia-Vidal and L. Martin-Moreno, *Dual Band Terahertz Waveguiding on a Planar Metal Surface patterned with Annular Holes.* Applied Physics Letters, 2010. **96**: p. 011101.

15. Ebbesen, T.W., et al., *Extraordinary opical transmission through sub-wavelength hole rarrays.* Nature, 1998. **391**: p. 667-669.

16. T.Thio, et al., *Surface lasmon-enhanced transmission throuh hole arrays in Cr films.* J. Opt. Soc. Am. B, 1999. **16**: p. 1743-1748.

17. P. G. Huggard, M.M., A. Schilz, K. Goller, and W. Prettl *Far-infrared bandpass filters from perforated metal screens.* Applied optics, 1994. **33**(1): p. 39-41.

18. Williams, C.R., et al., *Highly confined guiding of terahertz surface plasmon polaritons on structured metal surfaces.* Nature Photonics, 2008. **2**(3): p. 175-179.

19. Saleh, B.E., M.C. Teich, and B.E. Saleh, *Fundamentals of photonics.* Vol. 22. 1991: Wiley New York.

20. Maier, S.A., P.G. Kik, and H.A. Atwater, *Optical pulse propagation in metal nanoparticle chain waveguides.* Physical Review B, 2003. **67**(20): p. 205402.

21. Pendry, J.B., et al., *Magnetism from conductors and enhanced nonlinear phenomena.* IEEE transactions on microwave theory and techniques, 1999. **47**(11): p. 2075-2084.

22. Shelby, R.A., D.R. Smith, and S. Schultz, *Experimental verification of a negative index of refraction.* science, 2001. **292**(5514): p. 77-79.

23. Shalaev, V.M., et al., *Negative index of refraction in optical metamaterials.* Optics letters, 2005. **30**(24): p. 3356-3358.

24. Satoshi Yamauchi1*, S.H., Yoh Imai2, Masayoshi Tonouchi3, *Terahertz Time-Domain Spectroscopy to Identify and Evaluate Anomer in Lactose* American Journal of Analytical Chemistry, 2013. **2013**(4): p. 756-762.

25. Buckton, P.D.a.G., *The Influence of Heating:Drying on the Crystallisation of Amorphous Lactose after Structural Collapse.* International Journal of Pharmaceutics, 1997. **158**(2): p. 157-164.

26. Á. GombÁs, P.S.-R., M. Kata, J. G.I. Erős, *Quantitative Determination of Crystallinity of α-Lactose Monohydrate by DSC.* Journal of Thermal Analysis and Calorimetry, 2002. **68**(2): p. 503-510.

27. B. M. Murphya, S.W.P.a.I.L., *Measurement of Lactose Crystallinity Using Raman Spectroscopy.* Journal of Pharmaceutical and Biomedical Analysis, 2005. **38**(1): p. 186-190.

28. Roos, M.K.H.a.Y.H., *Lactose: A Definitive Guide to Polymorph Determination.* Carbohydrate Research, 2005. **340**(2): p. 293-301.

29. J. H. Kirk, S.E.D.a.C.G.B., *Lactose: A Definitive Guide to Polymorph Determination.* International Journal of Pharmaceutics, 2007. **334**(1-2): p. 103-114.

30. B Fischer, M.H., H Helm1, G Modjesch2 and P Uhd Jepsen, *Chemical recognition in terahertz time-domain spectroscopy and imaging.* Semiconductor Science and Technology, 2005. **20**(2005): p. 46-53.

31. Jon E. Bjarnason, E.R.B.a.T.M.K., *Comparison of the THz absorption feature in lactose to related saccharides.* Proceeding of SPIE, 2007. **6549**(2007): p. 1-9.

32. Demers, J.R. and R.T. Logan, *Method of Detecting Organic Materials Using Terahertz Spectroscopy*. 2011, Google Patents.